
Finding Optimal Tangent Points for Reducing Distortions of Hard-label Attacks

Chen Ma¹ Xiangyu Guo² Li Chen^{1,*} Jun-Hai Yong¹ Yisen Wang^{3,4}

¹ School of Software, BNRist, Tsinghua University, Beijing, China

² Department of Computer Science and Engineering, University at Buffalo, Buffalo NY, USA

³ Key Lab. of Machine Perception, School of Artificial Intelligence, Peking University, Beijing, China

⁴ Institute for Artificial Intelligence, Peking University, Beijing, China

machenstar@163.com, xiangyug@buffalo.edu

{chenlee,yongjh}@tsinghua.edu.cn, yisen.wang@pku.edu.cn

Abstract

One major problem in black-box adversarial attacks is the high query complexity in the hard-label attack setting, where only the top-1 predicted label is available. In this paper, we propose a novel geometric-based approach called Tangent Attack (TA), which identifies an optimal tangent point of a virtual hemisphere located on the decision boundary to reduce the distortion of the attack. Assuming the decision boundary is locally flat, we theoretically prove that the minimum ℓ_2 distortion can be obtained by reaching the decision boundary along the tangent line passing through such tangent point in each iteration. To improve the robustness of our method, we further propose a generalized method which replaces the hemisphere with a semi-ellipsoid to adapt to curved decision boundaries. Our approach is free of pre-training. Extensive experiments conducted on the ImageNet and CIFAR-10 datasets demonstrate that our approach can consume only a small number of queries to achieve the low-magnitude distortion. The implementation source code is released online at <https://github.com/machanic/TangentAttack>.

1 Introduction

Adversarial attacks cause deep neural networks (DNNs) to make incorrect predictions by slightly perturbing benign images during the test time. They can be divided into two main categories on the basis of the amount of information exposed by the target model, namely white-box and black-box attacks. Many white-box attacks [6, 30, 33] have been proposed, and they can compute the gradients w.r.t. the target model’s input images to generate adversarial examples with the first-order optimization techniques. In contrast, black-box attacks are more practical because they craft adversarial examples without requiring the target model’s gradients.

Over the past years, the community has made considerable efforts in developing black-box attacks, and the proposed methods can be divided into transfer- and query-based attacks. Transfer-based attacks [26, 40, 41] generate adversarial examples by using a white-box attack method against a surrogate model to fool the target model. Although there is no need to query the target model in these attacks, the attack success rate can not be guaranteed, especially in the case of targeted attacks. To achieve satisfactory attack success rates, the query-based attacks use elaborate queries to obtain the feedback of the target model for crafting adversarial examples. In the score-based setting, the query-based attacks [2, 12, 22, 29] estimate approximate gradients by querying the predicted scores of the target model at multiple points. However, in most real-world scenarios, the score-based setting

*Corresponding author.

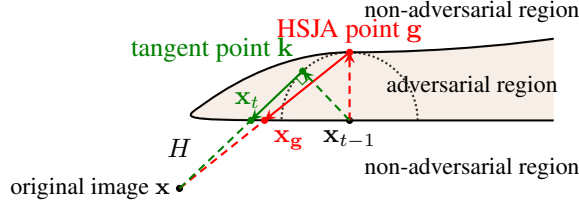


Figure 1: Simplified two-dimensional illustration of our motivation. H is the decision boundary, and \mathbf{x}_{t-1} is the current adversarial example mapped onto the decision boundary at the $(t-1)$ -th iteration. HSJA updates \mathbf{x}_{t-1} along the gradient direction to reach \mathbf{g} and then maps it to H at \mathbf{x}_g along the line through \mathbf{x} and \mathbf{g} . However, the optimal update should be the tangent point \mathbf{k} because it can be mapped onto H at \mathbf{x}_t that has the shortest distance to the original image \mathbf{x} .

is not applicable because the public service returns only the top-1 predicted label (*i.e.*, the hard label) rather than the predicted score. In this case, since the feedback information is limited and the objective function is discontinuous, the attack requires solving a high-dimensional combinatorial optimization problem, which is often challenging.

To reformulate the attack as a real-valued continuous optimization problem, OPT [10], Sign-OPT [11], and RayS [8] focus on minimizing an objective function $g(\theta)$, which is defined as the distance from the original image to the nearest adversarial example along the direction θ . However, when attacking complex models, it may be difficult to find a suitable direction θ along which adversarial examples exist.

Boundary Attack (BA) [4], HopSkipJumpAttack (HSJA) [7], QEBA [25], qFool [27], and Policy Driven Attack (PDA) [43] eliminate the search of the direction θ . Instead, they start from a large adversarial perturbation and then reduce its distortion while staying in the adversarial region. Because the output labels of the target model flip only near the decision boundary, these attacks restrict their explorations to the regions near the decision boundary. However, they do not thoroughly investigate the geometric properties of the decision boundary to accelerate the attack. For example, PDA uses a reinforcement learning framework to train a policy network to predict search directions, which are not geometrically optimal. In addition, the prediction accuracy of the policy network decreases significantly in the later stages of the iterations, resulting in worse performance of these iterations. HSJA and qFool simply use the gradient \mathbf{u} estimated at the decision boundary as the direction of each update, while ignoring a geometrically critical issue, *i.e.*, \mathbf{u} is not the optimal direction to be followed (Fig. 1). We could explore better search directions at each attack iteration.

To find the optimal search direction for minimizing the distortions of attack, we propose a new geometric-based approach whose motivation is illustrated in Fig. 1. We construct a virtual semicircle B centered at \mathbf{x}_{t-1} to indicate all possible locations that \mathbf{x}_{t-1} can reach along different directions, and the radius of B limits the range of updates for successful attacks. It is easy to observe that moving along the tangent line can reach the nearest location of the decision boundary to the original image \mathbf{x} , thereby producing the adversarial example with the minimum distortion. In real attack scenarios, the image data reside in a high-dimensional space, and the semicircle becomes a hemisphere. In this case, the benefit of using tangent points still exists, and we provide the detailed description and the formal proof in Section 3 and appendix.

To summarize, the main contributions of this study are as follows.

1. We cast the problem of minimizing the distortion in hard-label attacks into a geometric problem. We discover that the minimum distortion can be obtained by searching the optimal tangent point of a virtual hemisphere around the adversarial example at each iteration.
2. We propose a novel geometric-based method to obtain a closed-form solution of the optimal tangent point. We provide an intuitive explanation of our approach, as well as a formal proof of its correctness.
3. To improve robustness, we further propose a generalized method that replaces the hemisphere with a semi-ellipsoid to adapt to the target models with curved decision boundaries.
4. Extensive experiments conducted on the CIFAR-10 [24] and ImageNet [14] datasets demonstrate the effectiveness of our approach.

2 Related Work

Query-based black-box attacks can be divided into score- and decision-based attack (a.k.a. the hard-label attack). Score-based attacks [1, 2, 3, 9, 12, 22, 29, 32] use the predicted probability score to craft adversarial examples, which is not always available in most real-world systems. Hard-label attacks are more useful, but obviously more challenging, because only the top-1 predicted label can be obtained. The hard-label attacks usually fall into three categories.

The first category starts from the original image \mathbf{x}_0 and attempts to find an optimal direction θ to reach the adversarial example. OPT [10] searches an optimal θ to minimize the distance from \mathbf{x}_0 to the nearest adversarial example. Sign-OPT [11] improves the query efficiency of OPT by using a single query to estimate the sign of the directional derivative. RayS [8] eliminates the gradient estimation and proposes a fast check step to efficiently find the direction θ . However, RayS is only applicable to the untargeted attack under the ℓ_∞ norm because it is difficult to find a suitable direction to reach the region of the target class in a targeted attack, especially in the case of a large number of classes.

The second category starts from a large perturbation or an image of the target class, and then reduces its distortion while staying in adversarial region, thereby gradually making it closer to the original image. BA [4] and NES [1] are two representative methods, but they have high query complexity. Biased BA [5] reinterprets BA as a biased sampling framework and incorporates different biases to improve the query efficiency. HSJA [7] utilizes the gradient estimation and the binary search to outperform BA. HSJA can be used as the baseline of hard-label attacks. QEBA [25] improves HSJA by using dimension reduction techniques. SurFree [31] and GeoDA [34] improve the performance of HSJA by exploiting geometric properties of DNNs. However, the geometric features of DNNs have not been fully explored, and they do not support the targeted attack. PDA [43] uses a reinforcement learning framework to train a policy network to predict promising directions. However, PDA requires a high-cost pre-training, which is not always available in all tasks.

The third category uses a random sampling technique to improve query efficiency. Customized Adversarial Boundary (CAB) attack [37] uses the current noise to select the sensitive area of images and customize sampling distribution. Evolutionary [16] improves the query efficiency by reducing the dimension of the search space with the stochastic coordinate selection.

The issue of RayS and GeoDA is that they only support untargeted attacks. Because moving the original image far enough in any direction can always make it escape the non-adversarial region in untargeted attacks. However, in targeted attacks, it is difficult to find a suitable direction along which the target class’s region exists. In contrast, our approach supports all types of attacks, and we exploit the geometric characteristics of the decision boundaries of DNNs to boost the attack.

3 The Proposed Approach

3.1 The Goal of Hard-label Attacks

Given a target model $f : \mathbb{R}^d \rightarrow \mathbb{R}^k$ and a benign image $\mathbf{x} \in [0, 1]^d$ that is correctly classified using f , the goal of the adversary is to slightly perturb \mathbf{x} into \mathbf{x}_{adv} , such that $f(\mathbf{x}_{\text{adv}})$ outputs incorrect prediction. In the hard-label attack, the adversary can only observe the top-1 predicted label of f , denoted as $\hat{y} = \arg \max_i f(\mathbf{x}_{\text{adv}})_i$. We define an indicator function $\phi(\cdot)$ of a successful attack:

$$\phi(\mathbf{x}_{\text{adv}}) := \begin{cases} 1 & \text{if } \hat{y} = y_{\text{adv}} \text{ in the targeted attack,} \\ & \text{or } \hat{y} \neq y \text{ in the untargeted attack,} \\ 0 & \text{otherwise,} \end{cases} \quad (1)$$

where $y \in \mathbb{R}$ is the true label of \mathbf{x} and $y_{\text{adv}} \in \mathbb{R}$ is a predefined target class label. In this study, we focus on generating an adversarial example \mathbf{x}_{adv} that satisfies $\phi(\mathbf{x}_{\text{adv}}) = 1$, such that the distortion $d(\mathbf{x}_{\text{adv}}, \mathbf{x}) := \|\mathbf{x}_{\text{adv}} - \mathbf{x}\|_p$ is minimized. This goal can be formulated as the optimization problem:

$$\min_{\mathbf{x}_{\text{adv}}} d(\mathbf{x}_{\text{adv}}, \mathbf{x}) \quad \text{s.t.} \quad \phi(\mathbf{x}_{\text{adv}}) = 1. \quad (2)$$

3.2 Motivation

Most recent attacks belong to the second category (Section 2) follow a common procedure: it starts from an adversarial image yet not close enough to the benign one, then it iteratively searches for a

closer adversarial image. Let us take a typical attack HSJA [7] for example (Fig. 1). First, the attack initializes the adversarial example by using an image of the target class (in a targeted attack) or a noisy version of the original image (in an untargeted attack). Next, it performs the binary search to map the initial sample onto the decision boundary H , denoted as \mathbf{x}_{t-1} . Then, the algorithm iteratively performs three steps to update \mathbf{x}_{t-1} : estimating gradient \mathbf{u} at H by sampling many probes around \mathbf{x}_{t-1} ; jumping to the point \mathbf{g} along the direction \mathbf{u} with the step size determined by the geometric progression; and mapping \mathbf{g} onto H at \mathbf{x}_g by performing the binary search along the line passing through \mathbf{g} and the original image \mathbf{x} . However, geometrically speaking, the estimated gradient \mathbf{u} is not the optimal search direction, and we can find a better boundary point \mathbf{x}_t by connecting \mathbf{x} to a certain point on the semicircle B and then taking the intersection point on H . Fig. 1 shows that the tangent point \mathbf{k} is the optimum update because it leads to the minimum distortion of the attack.

3.3 Definition of Optimal Tangent Points

There is some experimental evidence that the decision boundaries of DNNs are smooth surfaces with the low curvature [17, 34]. Based on this observation, we approximate the local decision boundary with a hyperplane H . Fig. 3 illustrates our problem in three-dimensional space. We will derive our algorithm from \mathbb{R}^3 and show that it can be directly extended to higher-dimensional spaces. Lastly, we address the case of curved decision boundaries.

As described in Section 3.2, \mathbf{x}_{t-1} denotes the *boundary sample* that already lies on the decision boundary. We create a virtual hemisphere B centered at \mathbf{x}_{t-1} with a radius R , which is an estimation of the safe region where we can search for adversarial examples. In the targeted attack, B represents the current estimation of the target class region around \mathbf{x}_{t-1} . Ideally, B is small enough to be fully contained in the target class's region, i.e., $\phi(\mathbf{x}') = 1$ for $\forall \mathbf{x}' \in B$.

Then, we need to find a point on B which would produce the minimum distortion when mapped to H . In two-dimensional case, this point is the tangent point. However, in n -dimensional space where $n \geq 3$, there are infinitely many tangent lines of B passing through \mathbf{x} which create infinitely many tangent points on B , shown as the red points in Figs. 2 and 3. Still, we will show that exactly one tangent point can lead to the minimum distortion when mapping it onto H along the tangent line.

Formally, let \mathbf{k} be any point on the surface of B , \mathbf{u} be the approximate gradient of H estimated at \mathbf{x}_{t-1} , and \mathbf{x}_t be the intersection of H and the line passing through \mathbf{x} and \mathbf{k} , we have the following theorem.

Theorem 1. *Let H , \mathbf{u} , \mathbf{k} , \mathbf{x} , and \mathbf{x}_{t-1} be defined above, then the distance $\|\mathbf{x} - \mathbf{x}_t\|$ is minimized if \mathbf{k} is the optimal solution of the following constrained optimization problem:*

$$\arg \max_{\mathbf{k}} \langle \mathbf{k} - \mathbf{x}_{t-1}, \mathbf{u} \rangle \quad (3)$$

$$\text{s.t. } \langle \mathbf{k} - \mathbf{x}_{t-1}, \mathbf{x} - \mathbf{k} \rangle = 0, \quad (4)$$

$$\|\mathbf{k} - \mathbf{x}_{t-1}\| = R, \quad (5)$$

$$\langle \mathbf{k} - \mathbf{x}_{t-1}, \mathbf{u} \rangle \geq 0. \quad (6)$$

In particular, the optimal \mathbf{k} is in the plane spanned by \mathbf{u} and $\mathbf{x} - \mathbf{x}_{t-1}$.

The objective function of Eq. (3) is to maximize the projection of the vector $\mathbf{k} - \mathbf{x}_{t-1}$ onto \mathbf{u} , which is equivalent to finding \mathbf{k} that is farthest away from H . The first constraint ensures that \mathbf{k} is a tangent point. The second constraint indicates \mathbf{k} is on the surface of B . The last constraint states that \mathbf{k} cannot appear on the same side of H as \mathbf{x} , which is always satisfied if $\|\Pi_H(\mathbf{x} - \mathbf{x}_{t-1})\| \geq R$, where the notation $\Pi_H : \mathbb{R}^n \mapsto H$ denotes the orthogonal projection from \mathbb{R}^n onto the hyperplane H . If there is no feasible solution, then our algorithm (Algorithm 1) reduces the radius R to guarantee that the last constraint is always satisfied. The formal proof of Theorem 1 is presented in the appendix. Here,

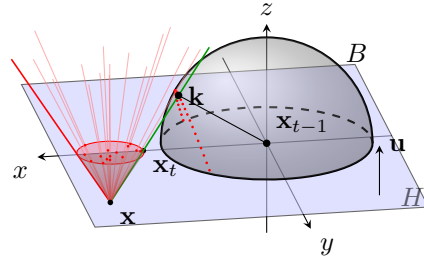


Figure 2: Geometrical explanation of Theorem 1. All points on H that are closer to \mathbf{x} than \mathbf{x}_t are within a red disk, which is the intersection of H and the red cone whose vertex is \mathbf{x} . Clearly \mathbf{k} is the only intersection point of the cone and the hemisphere B . Thus, of all the lines intersecting B , only the intersection of the tangent line and H is closest to \mathbf{x} .

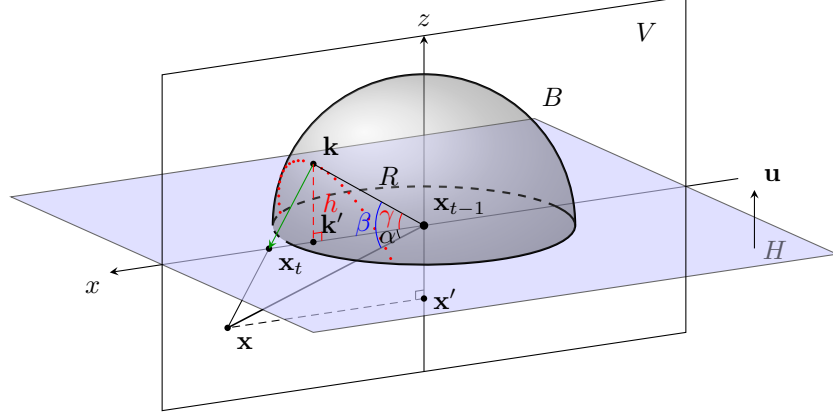


Figure 3: The illustration of the optimal tangent point \mathbf{k} for the flat decision boundary. The tangent point \mathbf{k} is on the surface of a virtual hemisphere B with a radius R centered at the adversarial example \mathbf{x}_{t-1} . \mathbf{x} is the original image, \mathbf{x}_t is the intersection point of the tangent line and the decision hyperplane H , \mathbf{k}' and \mathbf{x}' are the orthogonal projections of \mathbf{k} and \mathbf{x} onto H and z axis, respectively.

we refer the readers to Fig. 2 for an intuitive geometrical explanation. Eq. (3) is computationally expensive to solve in the high-dimensional space. Fortunately, we show there actually exists a closed-form solution.

3.4 Closed-Form Solution of the Optimal Tangent Point

The main intuition of the derivation is illustrated in Fig. 3, which shows an example in \mathbb{R}^3 . For ease of presentation, we move \mathbf{x}_{t-1} to $\mathbf{0}$. The known variables are \mathbf{x} , \mathbf{x}_{t-1} , the unit normal vector \mathbf{u} of hyperplane H , and the radius R . We need to solve for the unknown \mathbf{k} . Let $V = \text{span}(\{\mathbf{x}, \mathbf{u}\})$ be the plane spanned by \mathbf{x} and \mathbf{u} . According to Theorem 1, we know $\mathbf{k} \in V$. Let us denote the angle between \mathbf{x} and H as α , the angle between \mathbf{x} and \mathbf{k} as β , and the angle between \mathbf{k} and H as γ . Then, $\beta = \alpha + \gamma$ because all three points \mathbf{x} , \mathbf{k} , and \mathbf{x}_{t-1} are on the same plane V . Because the angle between \mathbf{x} and \mathbf{u} is $\pi/2 + \alpha$, we have

$$\langle \mathbf{x}, \mathbf{u} \rangle = \|\mathbf{x}\| \cdot \|\mathbf{u}\| \cdot \cos\left(\frac{\pi}{2} + \alpha\right) = \|\mathbf{x}\| \cdot \|\mathbf{u}\| \cdot (-\sin \alpha). \quad (7)$$

Then we have $\sin \alpha = -\frac{\langle \mathbf{x}, \mathbf{u} \rangle}{\|\mathbf{x}\| \cdot \|\mathbf{u}\|}$ and $\cos \alpha = \sqrt{1 - \sin^2 \alpha} = \frac{\sqrt{\|\mathbf{x}\|^2 \cdot \|\mathbf{u}\|^2 - \langle \mathbf{x}, \mathbf{u} \rangle^2}}{\|\mathbf{x}\| \cdot \|\mathbf{u}\|}$. By the constraint (4), $\mathbf{x} - \mathbf{k}$ is orthogonal to \mathbf{k} . Thus, we have $\cos \beta = R / \|\mathbf{x}\|$ and $\sin \beta = \sqrt{1 - \cos^2 \beta} = \sqrt{\|\mathbf{x}\|^2 - R^2} / \|\mathbf{x}\|$. Then $\sin \gamma$ and $\cos \gamma$ can be derived as functions of α and β from basic facts of trigonometric functions:

$$\begin{aligned} \sin \gamma &= \sin(\beta - \alpha) = \sin \beta \cos \alpha - \cos \beta \sin \alpha, \\ \cos \gamma &= \cos(\beta - \alpha) = \cos \beta \cos \alpha + \sin \beta \sin \alpha. \end{aligned} \quad (8)$$

Now, let $\mathbf{k}' \in H$ be the orthogonal projection of \mathbf{k} onto the plane H . The distance between \mathbf{k} and \mathbf{k}' is denoted as h (Fig. 3). Then $h = R \cdot \sin \gamma = R \cdot (\sin \beta \cos \alpha - \cos \beta \sin \alpha)$.

To derive \mathbf{k}' , let us denote \mathbf{x}' as the orthogonal projection of \mathbf{x} onto z axis. So we have $\mathbf{x}' = \langle \mathbf{x}, -\mathbf{u} \rangle \cdot (-\mathbf{u}) / \|\mathbf{u}\|^2 = \langle \mathbf{x}, \mathbf{u} \rangle \cdot \mathbf{u} / \|\mathbf{u}\|^2$. Then, because \mathbf{k}' and $\mathbf{x} - \mathbf{x}'$ are on the same direction, we have

$$\frac{\mathbf{k}'}{\|\mathbf{k}'\|} = \frac{\mathbf{x} - \mathbf{x}'}{\|\mathbf{x} - \mathbf{x}'\|}. \quad (9)$$

Now, $\|\mathbf{k}'\| = R \cdot \cos \gamma$ and $\mathbf{x}' = \langle \mathbf{x}, \mathbf{u} \rangle \cdot \mathbf{u} / \|\mathbf{u}\|^2$ are plugged into Eq. (9), and \mathbf{k}' is obtained as

$$\mathbf{k}' = \frac{\mathbf{x} - \mathbf{x}'}{\|\mathbf{x} - \mathbf{x}'\|} \cdot \|\mathbf{k}'\| = \frac{\mathbf{x} - \langle \mathbf{x}, \mathbf{u} \rangle \cdot \mathbf{u} / \|\mathbf{u}\|^2}{\|\mathbf{x} - \langle \mathbf{x}, \mathbf{u} \rangle \cdot \mathbf{u} / \|\mathbf{u}\|^2\|} \cdot R \cdot \cos \gamma. \quad (10)$$

Therefore, \mathbf{k} can be derived as

$$\mathbf{k} = \mathbf{k}' + h \cdot \mathbf{u} = \frac{\mathbf{x} - \langle \mathbf{x}, \mathbf{u} \rangle \cdot \mathbf{u} / \|\mathbf{u}\|^2}{\|\mathbf{x} - \langle \mathbf{x}, \mathbf{u} \rangle \cdot \mathbf{u} / \|\mathbf{u}\|^2\|} \cdot R \cdot \cos \gamma + h \cdot \mathbf{u}. \quad (11)$$

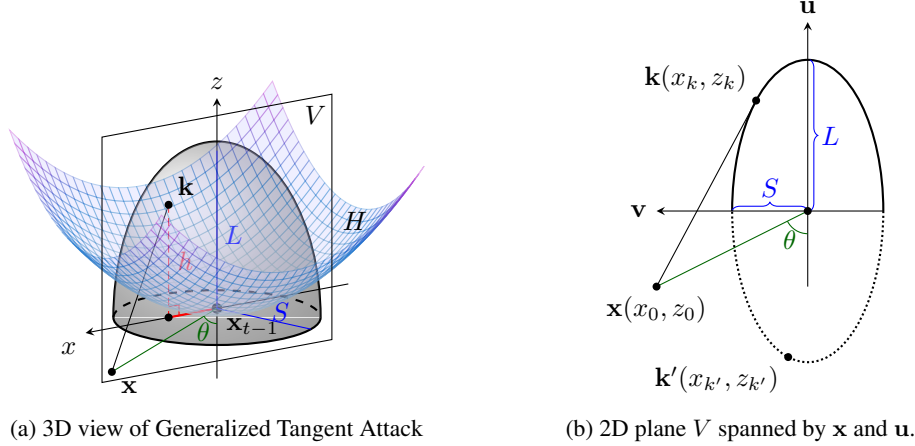


Figure 4: Illustration of the derivation of Generalized Tangent Attack, which replaces the hemisphere B with a semi-ellipsoid to increase the height of \mathbf{k} to adapt to curved decision boundaries.

Finally, because \mathbf{x}_{t-1} has been moved to the origin, we need to move \mathbf{k} back by adding \mathbf{x}_{t-1} .

We remark that although the above derivation is illustrated in \mathbb{R}^3 , it can be directly applied to higher dimensions. The reason is Theorem 1, which essentially reduces any dimension space to \mathbb{R}^2 : to find the optimal \mathbf{k} , we only need to focus on the plane V spanned by \mathbf{u} and $\mathbf{x} - \mathbf{x}_{t-1}$.

3.5 Generalized Tangent Attack

When the local decision boundary is not flat enough, the boundary point obtained via the tangent line may not be the optimal, as shown in Fig. 4a. A simple solution is to simply continue halving the radius R of the hemisphere: as long as R becomes small enough, the local flatness can always be obtained. However, too small a radius will reduce the convergence rate of our algorithm, because the distance between \mathbf{x}_t and \mathbf{x}_{t-1} is proportional to R . Therefore, when the classification decision boundary is a curved surface, the attack algorithm should change the shape of hemisphere rather than simply reducing R . Based on this idea, we propose the Generalized Tangent Attack (G-TA).

First, although the shape of the decision boundary can be very complex in a high-dimensional space, the important thing for our algorithm is only the situation in the two-dimensional plane spanned by \mathbf{x} and \mathbf{u} . In particular, if the decision boundary is “downward” curved (as opposed to the example in Fig. 4a), then searching along the tangent line is still a better approach than HSJA’s solution. Thus, the only “bad case” we have to deal with is when the decision boundary is “upward” curved and has a large curvature, as shown in Fig. 4a.

According to Theorem 1, we only need to focus on the plane V spanned by \mathbf{x} and \mathbf{u} , as shown in Fig. 4b. Now, \mathbf{u} and $\mathbf{v} := (\mathbf{x} - \langle \mathbf{x}, \mathbf{u} \rangle \cdot \mathbf{u} / \|\mathbf{u}\|^2) / \|\mathbf{x} - \langle \mathbf{x}, \mathbf{u} \rangle \cdot \mathbf{u} / \|\mathbf{u}\|^2\|$ form an orthogonal basis of the plane V , then \mathbf{x} can be identified with coordinates (x_0, z_0) , i.e., $\mathbf{x} = x_0\mathbf{v} + z_0\mathbf{u}$. Let θ denote the angle between the vector \mathbf{x} and the vector $-\mathbf{u}$, i.e., $\theta = \arccos\left(\frac{\langle \mathbf{x}, -\mathbf{u} \rangle}{\|\mathbf{x}\| \cdot \|\mathbf{u}\|}\right)$. Then $(x_0, z_0) = (\|\mathbf{x}\| \cdot \sin \theta, -\|\mathbf{x}\| \cdot \cos \theta)$. Consider the projection of the ellipsoid on V (which is an ellipse), we denote L as its radius along the direction of \mathbf{u} , and S as its radius along the direction of \mathbf{v} . Because the optimal tangent point \mathbf{k} lies in the plane V , \mathbf{k} can also be identified as $\mathbf{k} = x_k\mathbf{v} + z_k\mathbf{u}$, and we only need to solve for the unknown (x_k, z_k) .

The ellipse is characterized by the equation $x^2 / S^2 + z^2 / L^2 = 1$, thus the tangent point \mathbf{k} satisfies $x_k^2 / S^2 + z_k^2 / L^2 = 1$. Now we view z as a function of x , and take the derivative w.r.t. x at both sides of the equation to get the following formula:

$$\frac{2x_k}{S^2} + \frac{2z_k}{L^2} \cdot \frac{dz}{dx} \Big|_{x=x_k} = 0. \quad (12)$$

Thus, we have the slope of tangent line at \mathbf{k} be $\frac{dz}{dx} \Big|_{x=x_k} = -\frac{x_k L^2}{z_k S^2}$. Therefore, the tangent line can be written as $z - z_k = -\frac{x_k L^2}{z_k S^2}(x - x_k)$. Since the tangent line passes through \mathbf{x} , we know

$z_0 - z_k = -\frac{x_k L^2}{z_k S^2}(x_0 - x_k)$. In summary, we can obtain the following system of equations:

$$\begin{cases} L^2 x_k^2 + S^2 z_k^2 - x_k x_0 L^2 - z_0 z_k S^2 = 0, \\ \frac{x_k^2}{S} + \frac{z_k^2}{L} = 1. \end{cases} \quad (13)$$

In Eq. (13), the known variables are L, S, x_0 and z_0 , and the unknown variables that we need to solve for are x_k and z_k . In general, there are two solutions for Eq. (13), *i.e.*, \mathbf{k} and \mathbf{k}' depicted in Fig. 4b. Apparently, the solution of the optimal tangent point should satisfy $z_k > 0$, so the one of two solutions in which $z_k > 0$ should be picked:

$$\begin{cases} x_k = \frac{S^2 \left(L^2 - z_0 \cdot \frac{L^2 S^2 z_0 + L^2 x_0 \sqrt{-L^2 S^2 + L^2 x_0^2 + S^2 z_0^2}}{L^2 x_0^2 + S^2 z_0^2} \right)}{L^2 \cdot x_0}, \\ z_k = \frac{L^2 S^2 z_0 + L^2 x_0 \sqrt{-L^2 S^2 + L^2 x_0^2 + S^2 z_0^2}}{L^2 x_0^2 + S^2 z_0^2}. \end{cases} \quad (14)$$

Finally, the optimal tangent point \mathbf{k} is obtained via $\mathbf{k} = |x_k| \cdot \frac{\mathbf{x} - \langle \mathbf{x}, \mathbf{u} \rangle \cdot \mathbf{u} / \|\mathbf{u}\|^2}{\|\mathbf{x} - \langle \mathbf{x}, \mathbf{u} \rangle \cdot \mathbf{u} / \|\mathbf{u}\|^2\|} + z_k \cdot \mathbf{u}$. In the implementation, the value of L is determined in the same way as the radius R in TA (the hemisphere version). So we fix $L = R$, and use a hyperparameter $r = L/S$ to control the value of S . Imagine that in the case of \mathbb{R}^3 , the semi-ellipsoid becomes “slender” by setting $r > 1$, thereby adapting to the decision boundary of curved surface while preserving a relatively large step size.

3.6 The Complete Algorithm

TA (the hemisphere version) and G-TA (the semi-ellipsoid version) can be combined into one algorithm process, which is shown in Algorithm 1. It first performs a binary search to map the initial sample $\tilde{\mathbf{x}}_0$ to the decision boundary. Note that the binary search step always maps any \mathbf{x}_{adv} to the adversarial side of H that satisfies $\phi(\mathbf{x}_{\text{adv}}) = 1$, hence the attack success rate is always 100%. Then, it performs a *for* loop of T iterations to find the adversarial example that is close to \mathbf{x} . In the first iteration, we sample B_0 probes around the boundary sample to estimate the gradient, which is increased to $B_0 \sqrt{t}$ at the t -th iteration. This is because the error of gradient estimation in the later iterations has a greater impact on the attack performance, so using more samples can reduce the estimation error. Then, a *while* loop is performed to determine a reasonable radius R by repeatedly halving the radius until the tangent point \mathbf{k} is in the adversarial region. Finally, Algorithm 1 uses the binary search method to map \mathbf{k} back to the classification decision boundary to end this iteration.

Algorithm 1 Tangent Attack

Input: benign image \mathbf{x} , attack success indicator function $\phi(\cdot)$ defined in Eq. (1), initial batch size B_0 , iteration T , mode $m \in \{\text{semi-ellipsoid, hemisphere}\}$, radius ratio r .
Initialize $\tilde{\mathbf{x}}_0$ that satisfies $\phi(\tilde{\mathbf{x}}_0) = 1$;
 $\mathbf{x}_0 \leftarrow \text{BinarySearch}(\tilde{\mathbf{x}}_0, \mathbf{x}, \phi)$; ▷ boundary search
 $d_0 = \|\mathbf{x}_0 - \mathbf{x}\|$;
for t in $1, \dots, T$ **do**
 Sample $B_t \leftarrow B_0 \sqrt{t}$ random vectors to estimate the gradient \mathbf{u} ;
 Initialize $R \leftarrow d_{t-1} / \sqrt{t}$; ▷ the initial radius
 while true do
 Compute the optimal tangent point \mathbf{k} based on Eq. (11) **if** $m = \text{hemisphere}$ **else** Eq. (14);
 $R \leftarrow \frac{R}{2}$; ▷ search the radius, and we set $L = R, S = \frac{L}{r}$ if $m = \text{semi-ellipsoid}$
 if $\phi(\mathbf{k}) = 1$ **then**
 break;
 end if
 end while
 $\mathbf{k} \leftarrow \text{Clip}(\mathbf{k}, 0, 1)$;
 $\mathbf{x}_t \leftarrow \text{BinarySearch}(\mathbf{k}, \mathbf{x}, \phi)$; ▷ boundary search
 $d_t = \|\mathbf{x}_t - \mathbf{x}\|$;
end for

4 Experiment

4.1 Experimental Setting

Datasets. TA and G-TA are evaluated on two datasets, namely CIFAR-10 and ImageNet with the image resolutions of $32 \times 32 \times 3$ and $299 \times 299 \times 3$, respectively. We randomly select 1,000 correctly classified images from their validation sets for experiments.

Method Setting. The initial batch size B_0 is set to 100, which means the algorithm samples 100 probes for estimating a gradient at the first iteration. The threshold γ that controls the termination of the binary search is set to 1.0 in the CIFAR-10 dataset and 1,000 in the ImageNet dataset. The radius ratio r is set to 1.5 in the CIFAR-10 dataset and 1.1 in the ImageNet dataset. Besides, we also set r to 1.5 when attacking defense models. In targeted attacks, the target class label is set to $y_{adv} = (y + 1) \bmod C$, where y is the true label, and C is the number of classes.

Compared Methods. The advantage of our method is that it supports all types of attacks, including both untargeted and targeted attacks under ℓ_2 norm and ℓ_∞ norm constraints. Therefore, for complete and fair comparisons, we select the compared methods that support both untargeted and targeted attacks with state-of-the-art performance, including Boundary Attack (BA) [4], Sign-OPT [11], SVM-OPT [11], and HopSkipJumpAttack (HSJA) [7]. HSJA is adopted as the baseline, whose hyperparameters are set to be the same with ours (e.g. the same initial batch size B_0 and threshold γ). In addition, QEBA [25] is a HSJA-based method which has three variants: QEBA-I, QEBA-S and QEBA-F. We select QEBA-S in the additional experiment to verify whether the proposed method can improve attack performance of other HSJA-based method. For the consistency of experiments, we translate the implementations of Sign-OPT, SVM-OPT and HSJA from the official NumPy version into the PyTorch version by replacing each NumPy function with the corresponding PyTorch function. Thus, the two versions behave exactly the same. In the targeted attack, we randomly select an image from the target class of the validation set to be the initial sample of HSJA, BA, TA and G-TA. For fair comparison, we set the initial direction θ_0 of Sign-OPT and SVM-OPT to the direction of a randomly selected image of the target class. The detailed settings are presented in the appendix.

Target Models. In the CIFAR-10 dataset, we select four target models implemented using the PyTorch framework²: (1) a 272-layer PyramidNet+ShakeDrop network (PyramidNet-272) [19, 42] trained using AutoAugment [13]; (2) a model obtained through a neural architecture search called GDAS [15]; (3) a wide residual network with 28 layers and 10 times width expansion (WRN-28) [44]; and (4) a wide residual network with 40 layers (WRN-40) [44]. In the ImageNet dataset, we select four target models from an off-the-shelf library containing pre-trained weights³: (1) Inception-v3 [39], (2) Inception-v4 [38], (3) ResNet-101 [20], and (4) SENet-154 [21].

Evaluation Metric. Following previous studies [43], we report the mean ℓ_2 distortions as $\frac{1}{|\mathbf{X}|} \sum_{\mathbf{x} \in \mathbf{X}} (\|\mathbf{x}_{adv} - \mathbf{x}\|)$ under different query budgets, where \mathbf{X} is the test set.

4.2 Comparisons with State-of-the-Art Methods

Results of Attacks against Undefended Models. Tables 1 and 2 show the experimental results on the ImageNet and CIFAR-10 datasets. We derive two conclusions based on the results:

(1) We found that the experiments of CIFAR-10 requires a larger radius ratio r than that of ImageNet to achieve the satisfactory performance of G-TA. We speculate that the reason is that the target models of ImageNet have relatively flat decision boundaries.

(2) TA is more effective in targeted attacks, while the G-TA performs better in untargeted ones. This is because the adversarial region of the target class is narrower and more scattered, making the local classification decision boundary smoother, so that Theorem 1 holds and TA performs better.

In addition, one unique benefit of our approach is that it can be used as a performance enhanced plug-in when combining it with other HSJA-based approaches (e.g., QEBA-S). Specifically, the method is to change the jump directions of boundary samples of QEBA-S to the directions of the optimal tangent points. We present that “QEBA-S + TA” can further improve the performance of QEBA-S, as shown in Table 3.

²Pre-trained weights: <https://github.com/machanic/SimulatorAttack>

³Pre-trained weights: <https://github.com/Cadene/pretrained-models.pytorch>

Table 1: Mean ℓ_2 distortions of different query budgets on the ImageNet dataset, where $r = 1.1$.

Target Model	Method	Targeted Attack						Untargeted Attack					
		@300	@1K	@2K	@5K	@8K	@10K	@300	@1K	@2K	@5K	@8K	@10K
Inception-v3	BA [4]	111.798	108.044	106.283	102.715	86.931	78.326	-	107.558	102.309	95.776	78.668	60.296
	Sign-OPT [11]	103.939	87.706	71.291	46.744	34.640	29.414	121.085	79.158	43.642	16.625	10.557	8.680
	SVM-OPT [11]	101.630	82.950	67.965	46.275	35.694	31.106	121.135	66.027	36.763	15.736	10.501	8.789
	HSJA [7]	111.562	95.295	82.111	52.544	37.395	30.425	103.605	57.295	37.185	15.484	9.989	7.967
	TA	103.781	80.327	66.708	42.121	30.846	25.566	94.752	52.523	35.229	15.040	9.748	7.793
	G-TA	103.724	81.089	67.168	42.434	31.011	25.587	94.668	52.037	34.540	14.643	9.540	7.618
Inception-v4	BA [4]	110.343	106.616	104.586	100.321	84.058	75.507	-	116.075	111.474	104.451	86.572	66.283
	Sign-OPT [11]	101.620	85.731	69.719	46.416	34.957	30.004	132.991	86.431	48.292	18.678	11.567	9.262
	SVM-OPT [11]	99.856	81.342	66.982	45.667	35.477	31.152	132.227	72.920	41.095	17.611	11.418	9.372
	HSJA [7]	109.670	93.916	80.937	52.358	37.773	30.958	110.727	63.731	42.290	17.936	11.367	8.911
	TA	101.666	78.683	65.304	41.629	30.993	25.958	101.207	58.616	40.314	17.639	11.304	8.907
	G-TA	101.495	79.210	65.888	42.002	30.965	25.847	101.173	58.225	39.788	17.265	11.008	8.677
SENet-154	BA [4]	81.090	77.723	76.122	71.967	55.953	47.652	-	75.998	71.671	66.983	53.917	40.725
	Sign-OPT [11]	75.722	62.876	49.191	30.155	21.333	17.672	70.035	47.705	27.314	10.890	6.643	5.245
	SVM-OPT [11]	74.658	58.677	46.827	30.264	22.461	19.186	69.854	40.291	23.692	10.494	6.666	5.409
	HSJA [7]	77.035	63.488	51.802	30.138	19.680	16.261	71.248	38.035	24.895	10.218	5.855	4.842
	TA	70.739	55.256	43.694	24.961	16.756	13.876	65.589	35.689	24.037	10.039	5.774	4.766
	G-TA	70.591	55.224	44.047	25.041	16.854	14.047	65.871	35.768	23.954	9.959	5.733	4.734
ResNet-101	BA [4]	81.565	77.903	76.366	72.392	58.746	51.679	-	64.007	60.389	56.544	44.175	31.371
	Sign-OPT [11]	76.732	63.939	51.231	32.439	23.160	19.248	56.244	38.282	21.985	10.048	7.050	6.050
	SVM-OPT [11]	77.031	61.417	49.842	32.806	24.553	20.964	55.894	32.638	19.409	9.830	7.185	6.281
	HSJA [7]	76.121	63.091	52.301	31.018	20.472	16.911	56.264	27.443	17.717	7.649	4.723	4.019
	TA	72.434	57.969	47.142	27.699	18.788	15.414	53.197	26.777	17.651	7.730	4.822	4.107
	G-TA	72.459	58.320	47.297	27.905	19.045	15.633	53.058	26.631	17.384	7.602	4.720	4.026

Table 2: Mean ℓ_2 distortions with different query budgets on the CIFAR-10 dataset, where $r = 1.5$.

Target Model	Method	Targeted Attack						Untargeted Attack					
		@300	@1K	@2K	@5K	@8K	@10K	@300	@1K	@2K	@5K	@8K	@10K
PyramidNet-272	BA [4]	8.651	8.073	8.013	6.387	4.189	3.333	-	5.636	4.725	4.414	2.750	1.696
	Sign-OPT [11]	8.279	6.331	4.250	1.718	0.960	0.718	4.387	2.334	1.178	0.403	0.267	0.226
	SVM-OPT [11]	9.207	6.801	4.530	2.010	1.207	0.947	4.481	2.318	1.093	0.414	0.276	0.236
	HSJA [7]	7.917	4.329	2.523	0.793	0.489	0.397	4.505	1.279	0.713	0.333	0.255	0.227
	TA	7.943	4.267	2.488	0.809	0.503	0.406	4.256	1.275	0.710	0.329	0.253	0.226
	G-TA	7.816	4.277	2.469	0.803	0.505	0.412	4.432	1.270	0.702	0.329	0.252	0.225
GDAS	BA [4]	8.487	7.885	7.821	6.034	3.632	2.703	-	2.717	2.514	2.373	1.642	1.106
	Sign-OPT [11]	8.372	6.514	4.351	1.827	0.987	0.711	4.917	4.159	3.260	1.352	0.452	0.250
	SVM-OPT [11]	9.529	7.243	5.092	2.347	1.317	0.958	4.909	3.950	2.736	1.082	0.371	0.234
	HSJA [7]	7.714	3.566	1.966	0.591	0.365	0.301	2.188	0.756	0.483	0.261	0.208	0.189
	TA	7.674	3.529	1.946	0.585	0.366	0.302	2.190	0.774	0.485	0.257	0.206	0.187
	G-TA	7.697	3.558	1.959	0.583	0.361	0.298	2.161	0.745	0.476	0.255	0.204	0.185
WRN-28	BA [4]	8.688	8.046	7.984	5.786	2.486	1.555	-	4.425	3.648	3.435	1.543	0.832
	Sign-OPT [11]	8.258	5.576	3.260	1.087	0.593	0.459	3.093	1.494	0.828	0.319	0.239	0.213
	SVM-OPT [11]	9.516	5.968	3.744	1.367	0.728	0.553	2.977	1.466	0.723	0.325	0.245	0.221
	HSJA [7]	6.810	2.603	1.326	0.518	0.389	0.347	3.052	0.797	0.508	0.299	0.250	0.232
	TA	6.802	2.556	1.311	0.519	0.394	0.353	2.974	0.785	0.496	0.293	0.249	0.233
	G-TA	6.755	2.543	1.281	0.513	0.387	0.345	2.995	0.782	0.502	0.298	0.250	0.232
WRN-40	BA [4]	8.658	8.014	7.953	5.738	2.484	1.566	-	4.377	3.586	3.367	1.487	0.821
	Sign-OPT [11]	8.156	5.579	3.300	1.186	0.646	0.501	4.754	3.239	1.885	0.311	0.226	0.201
	SVM-OPT [11]	9.339	6.061	3.840	1.445	0.800	0.605	4.457	2.756	0.739	0.310	0.229	0.206
	HSJA [7]	6.909	2.648	1.330	0.528	0.400	0.357	2.992	0.777	0.498	0.290	0.242	0.225
	TA	6.944	2.579	1.295	0.523	0.398	0.358	2.926	0.770	0.490	0.288	0.243	0.227
	G-TA	6.783	2.605	1.320	0.535	0.403	0.361	2.952	0.772	0.492	0.288	0.241	0.223

Table 3: Experimental results of the combined method of QEBA-S and TA.

Target Model	Method	Targeted Attack					
		@300	@1K	@2K	@5K	@8K	@10K
Inception-v3	QEBA-S [25]	100.295	79.604	63.621	35.194	22.773	18.414
	QEBA-S + TA	104.490	75.622	59.836	33.112	22.329	17.799
Inception-v4	QEBA-S [25]	97.772	77.347	62.451	35.275	23.204	19.002
	QEBA-S + TA	101.845	73.838	58.554	33.288	23.160	18.736
SENet-154	QEBA-S [25]	72.831	55.367	42.674	21.988	13.888	11.210
	QEBA-S + TA	76.547	52.269	39.740	20.608	13.873	11.016
ResNet-101	QEBA-S [25]	75.567	57.929	44.983	23.209	14.402	11.467
	QEBA-S + TA	78.709	53.917	41.245	21.198	13.856	10.773

Results of Attacks against Defense Models. We conduct the experiments of untargeted attacks on defense models. Fig. 5 shows the experimental results on the CIFAR-10 dataset. We select 4 defense models: (1) a model obtained through adversarial training, abbreviated as AT [30]; (2) an

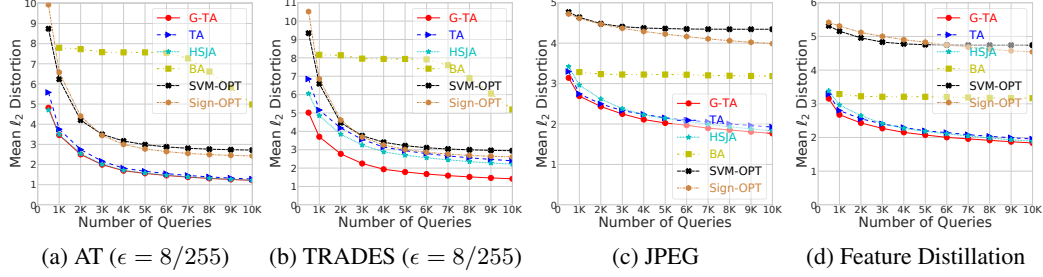


Figure 5: Experimental results of the attacks against defense models with the backbone of ResNet-50.

improved AT that optimizes a regularized surrogate loss, named as TRADES [46]; (3) an image-transformation-based defense called JPEG [18]; and (4) a DNN-oriented compression defense called Feature Distillation [28]. All defense models adopt ResNet-50 as the backbone. Previous studies [47] have shown that AT and TRADES have the issue of robust overfitting, which leads to a significant increase in the curvature of the classification decision boundary. Fig. 5b shows that G-TA performs best in attacking TRADES. This advantage is also demonstrated in attacking other defenses (*e.g.*, Fig. 5d), proving the effectiveness of G-TA in attacking the models with curved decision boundaries.

4.3 Comprehensive Understanding of Tangent Attack

In the ablation studies, we conduct the experiments of the targeted attacks on the ImageNet dataset to understand our approach in depth, and the target model is ResNet-50. The results are shown in Fig. 6.

Initialization. Our algorithm starts with an image \tilde{x}_0 selected from the target class, and we study three selection strategies: (1) a randomly selected image, (2) the image with the shortest distance to the original image, and (3) the image with the longest distance to the original image. Fig. 6a shows that the strategy of (2) achieves the best performance.

Radius Ratio. Fig. 6b shows that the performance of G-TA is not sensitive to the radius ratio r .

Jump Direction. Fig. 6c shows the effects of different jump directions. RandomHSJA is a variant of HSJA which adopts a random vector \mathbf{r} that satisfies $\langle \mathbf{r}, \mathbf{u} \rangle > 0$ as the jump direction. Fig. 6c verifies the benefit of jumping to the optimal tangent point.

Initial Batch Size. In general, Fig. 6d shows that a smaller B_0 performs better since it saves queries. But $B_0 = 5$ performs worse than $B_0 = 30$ because it uses too few samples for gradient estimation.

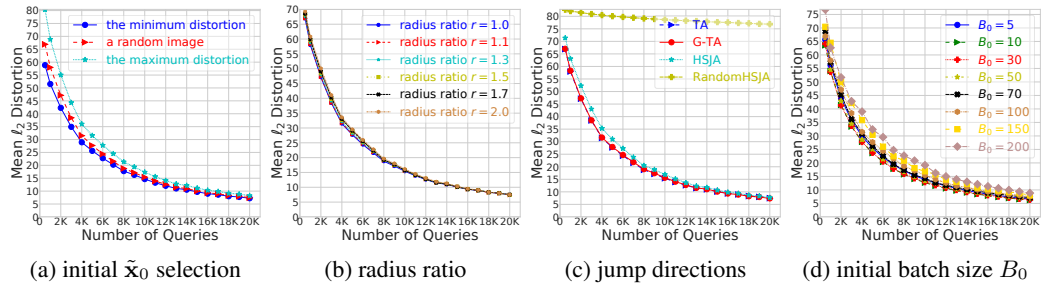


Figure 6: Experimental results of ablation studies.

5 Conclusion

In this paper, we propose a new geometric-based method for query-efficient hard-label black-box attacks. Our method relies on the observation that the minimum ℓ_2 distortion can be obtained by searching a boundary point along a tangent line of a virtual hemisphere. We offer a closed-form solution for computing the optimal tangent point and provide a formal proof of its correctness. We further propose a generalized method that replaces the hemisphere with a semi-ellipsoid to adapt to the target models with curved decision boundaries. Lastly, we evaluate our approach through extensive experiments and show its superior performance compared with baseline methods.

Acknowledgments

This research is partially supported by the National Key R&D Program of China (2019YFB1405703) and TC190A4DA/3, the National Natural Science Foundation of China (Grant Nos. 62021002, 61972221). Yisen Wang is partially supported by the National Natural Science Foundation of China under Grant 62006153, and Project 2020BD006 supported by PKU-Baidu Fund.

References

- [1] Ilyas Andrew, Engstrom Logan, Athalye Anish, and Lin Jessy. Black-box adversarial attacks with limited queries and information. In *International Conference on Machine Learning*, pages 2142–2151, 2018.
- [2] Yang Bai, Yuyuan Zeng, Yong Jiang, Yisen Wang, Shu-Tao Xia, and Weiwei Guo. Improving query efficiency of black-box adversarial attack. In *European Conference on Computer Vision*, pages 101–116, 2020.
- [3] Arjun Nitin Bhagoji, Warren He, Bo Li, and Dawn Song. Practical black-box attacks on deep neural networks using efficient query mechanisms. In *European Conference on Computer Vision*, pages 158–174, 2018.
- [4] Wieland Brendel, Jonas Rauber, and Matthias Bethge. Decision-based adversarial attacks: reliable attacks against black-box machine learning models. In *International Conference on Learning Representations*, pages 1–12, 2018.
- [5] T. Brunner, F. Diehl, M. T. Le, and A. Knoll. Guessing smart: biased sampling for efficient black-box adversarial attacks. In *IEEE/CVF International Conference on Computer Vision*, pages 4957–4965, 2019.
- [6] Nicholas Carlini and David A. Wagner. Towards evaluating the robustness of neural networks. In *IEEE Symposium on Security and Privacy*, pages 39–57, 2017.
- [7] Jianbo Chen, Jordan Michael L., and Wainwright Martin J. HopSkipJumpAttack: a query-efficient decision-based adversarial attack. In *IEEE Symposium on Security and Privacy*, pages 1277–1294, 2020.
- [8] Jinghui Chen and Quanquan Gu. RayS: a ray searching method for hard-label adversarial attack. In *ACM SIGKDD International Conference on Knowledge Discovery and Data Mining*, page 1739–1747, 2020.
- [9] Pin-Yu Chen, Huan Zhang, Yash Sharma, Jinfeng Yi, and Cho-Jui Hsieh. ZOO: zeroth order optimization based black-box attacks to deep neural networks without training substitute models. In *ACM Workshop on Artificial Intelligence and Security*, pages 15–26, 2017.
- [10] Minhao Cheng, Thong Le, Pin-Yu Chen, Huan Zhang, JinFeng Yi, and Cho-Jui Hsieh. Query-efficient hard-label black-box attack: an optimization-based approach. In *International Conference on Learning Representations*, pages 1–14, 2019.
- [11] Minhao Cheng, Simranjit Singh, Pin-Yu Chen, Sijia Liu, and Cho-Jui Hsieh. Sign-OPT: a query-efficient hard-label adversarial attack. In *International Conference on Learning Representations*, pages 1–16, 2020.
- [12] Shuyu Cheng, Yinpeng Dong, Tianyu Pang, Hang Su, and Jun Zhu. Improving black-box adversarial attacks with a transfer-based prior. In *Advances in Neural Information Processing Systems*, pages 10934–10944, 2019.
- [13] Ekin D Cubuk, Barret Zoph, Dandelion Mane, Vijay Vasudevan, and Quoc V Le. AutoAugment: learning augmentation strategies from data. In *IEEE/CVF Conference on Computer Vision and Pattern Recognition*, pages 113–123, 2019.
- [14] Jia Deng, Wei Dong, Richard Socher, Li-Jia Li, Kai Li, and Li Fei-Fei. ImageNet: a large-scale hierarchical image database. In *IEEE Conference on Computer Vision and Pattern Recognition*, pages 248–255, 2009.
- [15] Xuanyi Dong and Yi Yang. Searching for a robust neural architecture in four GPU hours. In *IEEE/CVF Conference on Computer Vision and Pattern Recognition*, pages 1761–1770, 2019.
- [16] Yinpeng Dong, Hang Su, Baoyuan Wu, Zhifeng Li, Wei Liu, Tong Zhang, and Jun Zhu. Efficient decision-based black-box adversarial attacks on face recognition. In *IEEE/CVF Conference on Computer Vision and Pattern Recognition*, pages 7714–7722, 2019.
- [17] Alhussein Fawzi, Seyed-Mohsen Moosavi-Dezfooli, and Pascal Frossard. Robustness of classifiers: from adversarial to random noise. In *Advances in Neural Information Processing Systems*, page 1632–1640, 2016.

- [18] Chuan Guo, Mayank Rana, Moustapha Cisse, and Laurens van der Maaten. Countering adversarial images using input transformations. In *International Conference on Learning Representations*, pages 1–12, 2018.
- [19] Dongyoon Han, Jiwhan Kim, and Junmo Kim. Deep pyramidal residual networks. In *IEEE Conference on Computer Vision and Pattern Recognition*, pages 5927–5935, 2017.
- [20] Kaiming He, Xiangyu Zhang, Shaoqing Ren, and Jian Sun. Deep residual learning for image recognition. In *IEEE Conference on Computer Vision and Pattern Recognition*, pages 770–778, 2016.
- [21] Jie Hu, Li Shen, and Gang Sun. Squeeze-and-excitation networks. In *IEEE/CVF Conference on Computer Vision and Pattern Recognition*, pages 7132–7141, 2018.
- [22] Andrew Ilyas, Logan Engstrom, and Aleksander Madry. Prior convictions: black-box adversarial attacks with bandits and priors. In *International Conference on Learning Representations*, pages 1–25, 2019.
- [23] Xiaojun Jia, Xingxing Wei, Xiaochun Cao, and Hassan Foroosh. ComDefend: an efficient image compression model to defend adversarial examples. In *IEEE/CVF Conference on Computer Vision and Pattern Recognition*, pages 6084–6092, 2019.
- [24] Alex Krizhevsky. Learning multiple layers of features from tiny images. pages 1–60, 2009.
- [25] Huichen Li, Xiaojun Xu, Xiaolu Zhang, Shuang Yang, and Bo Li. QEBA: Query-efficient boundary-based blackbox attack. In *IEEE/CVF Conference on Computer Vision and Pattern Recognition*, pages 1221–1230, 2020.
- [26] Yanpei Liu, Xinyun Chen, Chang Liu, and Dawn Song. Delving into transferable adversarial examples and black-box attacks. In *International Conference on Learning Representations*, pages 1–24, 2017.
- [27] Yujia Liu, Seyed-Mohsen Moosavi-Dezfooli, and Pascal Frossard. A geometry-inspired decision-based attack. In *IEEE/CVF International Conference on Computer Vision*, pages 4889–4897, 2019.
- [28] Zihao Liu, Qi Liu, Tao Liu, Nuo Xu, Xue Lin, Yanzhi Wang, and Wujie Wen. Feature distillation: DNN-oriented jpeg compression against adversarial examples. In *IEEE/CVF Conference on Computer Vision and Pattern Recognition*, pages 860–868, 2019.
- [29] Chen Ma, Li Chen, and Jun-Hai Yong. Simulating unknown target models for query-efficient black-box attacks. In *IEEE/CVF Conference on Computer Vision and Pattern Recognition*, pages 11835–11844, 2021.
- [30] Aleksander Madry, Aleksandar Makelov, Ludwig Schmidt, Dimitris Tsipras, and Adrian Vladu. Towards deep learning models resistant to adversarial attacks. In *International Conference on Learning Representations*, pages 1–28, 2018.
- [31] Thibault Maho, Teddy Furon, and Erwan Le Merrer. SurFree: a fast surrogate-free black-box attack. In *IEEE/CVF Conference on Computer Vision and Pattern Recognition*, pages 10430–10439, 2021.
- [32] Seungyong Moon, Gaon An, and Hyun Oh Song. Parsimonious black-box adversarial attacks via efficient combinatorial optimization. In *International Conference on Machine Learning*, pages 4636–4645, 2019.
- [33] Seyed-Mohsen Moosavi-Dezfooli, Alhussein Fawzi, and Pascal Frossard. DeepFool: a simple and accurate method to fool deep neural networks. In *IEEE Conference on Computer Vision and Pattern Recognition*, pages 2574–2582, 2016.
- [34] Ali Rahmati, Seyed-Mohsen Moosavi-Dezfooli, Pascal Frossard, and Huaiyu Dai. GeoDA: a geometric framework for black-box adversarial attacks. In *IEEE/CVF Conference on Computer Vision and Pattern Recognition*, pages 8446–8455, 2020.
- [35] Jonas Rauber, Wieland Brendel, and Matthias Bethge. Foolbox: a Python toolbox to benchmark the robustness of machine learning models. In *Reliable Machine Learning in the Wild Workshop of International Conference on Machine Learning*, pages 1–6, 2017.
- [36] Jonas Rauber, Roland Zimmermann, Matthias Bethge, and Wieland Brendel. Foolbox Native: fast adversarial attacks to benchmark the robustness of machine learning models in PyTorch, TensorFlow, and JAX. *Journal of Open Source Software*, 5(53):2607, 2020.
- [37] Yucheng Shi, Yahong Han, and Qi Tian. Polishing decision-based adversarial noise with a customized sampling. In *IEEE/CVF Conference on Computer Vision and Pattern Recognition*, pages 1030–1038, 2020.

- [38] Christian Szegedy, Sergey Ioffe, Vincent Vanhoucke, and Alexander Alemi. Inception-v4, inception-resnet and the impact of residual connections on learning. In *AAAI Conference on Artificial Intelligence*, page 4278–4284, 2017.
- [39] Christian Szegedy, Vincent Vanhoucke, Sergey Ioffe, Jon Shlens, and Zbigniew Wojna. Rethinking the inception architecture for computer vision. In *IEEE Conference on Computer Vision and Pattern Recognition*, pages 2818–2826, 2016.
- [40] Xin Wang, Jie Ren, Shuyun Lin, Xiangming Zhu, Yisen Wang, and Quanshi Zhang. A unified approach to interpreting and boosting adversarial transferability. In *International Conference on Learning Representations*, pages 1–35, 2021.
- [41] Dongxian Wu, Yisen Wang, Shu-Tao Xia, James Bailey, and Xingjun Ma. Skip connections matter: on the transferability of adversarial examples generated with ResNets. In *International Conference on Learning Representations*, pages 1–15, 2020.
- [42] Yoshihiro Yamada, Masakazu Iwamura, Takuya Akiba, and Koichi Kise. Shakedown regularization for deep residual learning. *IEEE Access*, 7:186126–186136, 2019.
- [43] Ziang Yan, Yiwen Guo, Jian Liang, and Changshui Zhang. Policy-driven attack: learning to query for hard-label black-box adversarial examples. In *International Conference on Learning Representations*, pages 1–15, 2021.
- [44] Sergey Zagoruyko and Nikos Komodakis. Wide residual networks. In *British Machine Vision Conference*, pages 87.1–87.12, 2016.
- [45] Haichao Zhang and Jianyu Wang. Defense against adversarial attacks using feature scattering-based adversarial training. In *Advances in Neural Information Processing Systems*, pages 1829–1839, 2019.
- [46] Hongyang Zhang, Yaodong Yu, Jiantao Jiao, Eric Xing, Laurent El Ghaoui, and Michael Jordan. Theoretically principled trade-off between robustness and accuracy. In *International Conference on Machine Learning*, pages 7472–7482, 2019.
- [47] Jingfeng Zhang, Jianing Zhu, Gang Niu, Bo Han, Masashi Sugiyama, and Mohan Kankanhalli. Geometry-aware instance-reweighted adversarial training. In *International Conference on Learning Representations*, pages 1–29, 2021.

Appendix

A Potential Negative Societal Impacts

The adversarial attack is a major security concern in the real-world machine learning system, because the generated adversarial perturbation could be used for the malicious purpose. Our study relies only on the top-1 predicted label to craft the adversarial examples which is applicable to most real-world systems, making it more useful and practical. Although the experiments in this paper are about attacking the image classifier, this method can be used in other settings, such as the object detection, the recommender system, the facial recognition system, and the autonomous driving. In summary, this study could be used in harmful ways by malicious users.

In a broader perspective, the adversarial example is not restricted to malicious applications, and it can be used in the positive side, *e.g.*, the generation of CAPTCHA and the privacy protection. In particular, the study of adversarial attacks can promote the defense techniques. In recent years, many proposed defenses are broken by the latest attacks, which stimulates the development of defenses.

Our results also point to the potential defense techniques against hard-label attacks. For example, the defense can prohibit queries near the decision boundary, then the approximate gradient cannot be estimated, making Tangent Attack ineffective. Another possible defense is to add random perturbations to the input image to prevent effective gradient estimation, or predict random classification labels for samples near the classification decision boundary.

B Proof of Theorem 1

B.1 Notations and Assumption

Before we formally prove Theorem 1, let us first define the notations that will be used in the proof. Let \mathbf{x} denote the original image, and w.l.o.g. we assume the boundary sample $\mathbf{x}_{t-1} = \mathbf{0}$ be the origin of the coordinate axis. Let B denote a n -dimensional ball centered at \mathbf{x}_{t-1} with the radius of R , and its surface is denoted as $S := \partial B$. Note that B denotes a complete ball in this proof. However, B denotes the hemisphere in the main text of the paper. Theorem 1 assumes that the classification decision boundary of the target model is the hyperplane H , which is defined by its unit normal vector \mathbf{u} . Then, the hyperplane H divides \mathbb{R}^n into two half-spaces:

$$\begin{aligned} H_{\geq 0} &= \{\mathbf{v} \in \mathbb{R}^n \mid \langle \mathbf{v}, \mathbf{u} \rangle \geq 0\}, \\ H_{\leq 0} &= \{\mathbf{v} \in \mathbb{R}^n \mid \langle \mathbf{v}, \mathbf{u} \rangle \leq 0\}. \end{aligned} \tag{15}$$

In the attack, $H_{\geq 0}$ mainly contains the adversarial region, and $H_{\leq 0}$ represents the non-adversarial region. In Fig. 7, we visually represent the hyperplane H and two half-spaces in \mathbb{R}^3 .

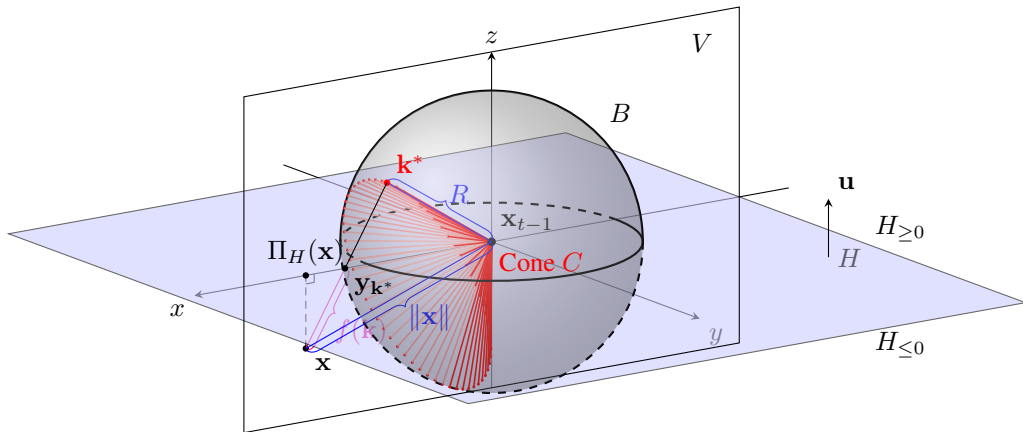


Figure 7: Illustration of the entities defined in the proof, where C is a convex cone whose boundary intersects with the circle formed by all the tangent points from \mathbf{x} to the ball B .

Suppose $\mathbf{x} \in H_{\leq 0} \setminus B$ is a fixed point outside B such that $\langle \mathbf{x}, \mathbf{u} \rangle < 0$. Now, let us define the cosine function $\cos(\mathbf{a}, \mathbf{b}) := \frac{\langle \mathbf{a}, \mathbf{b} \rangle}{\|\mathbf{a}\| \|\mathbf{b}\|}$ to represent the cosine of the angle between two vectors, then we can define the convex cone C with \mathbf{x}_{t-1} as its vertex, as shown below:

$$C := \left\{ \mathbf{v} \in \mathbb{R}^n \mid \cos(\mathbf{v}, \mathbf{x}) \geq \frac{R}{\|\mathbf{x}\|} \right\}. \quad (16)$$

Fig. 7 demonstrates the convex cone C in \mathbb{R}^3 . For $\mathbf{v} \in S \cap C$ that satisfies $\cos(\mathbf{v}, \mathbf{x}) = R / \|\mathbf{x}\|$, the equation $\|\mathbf{v} - \mathbf{x}\|^2 = \|\mathbf{x}\|^2 - \|\mathbf{v}\|^2$ holds, *i.e.*, \mathbf{v} is the tangent point of the tangent line from \mathbf{x} to the surface of B .

To make the feasible region of the optimization problem (3) in Theorem 1 nonempty, we need to make an assumption about the positional relationship between \mathbf{x} and the ball B . Let $\Pi_H : \mathbb{R}^n \mapsto H$ denote the orthogonal projection from \mathbb{R}^n onto the hyperplane H , we make the following assumption:

Assumption B.1. $\Pi_H(\mathbf{x}) \in C$

Note that Assumption B.1 is not really an ‘‘assumption’’: it essentially means that there is a tangent point on $S \cap H_{\geq 0}$, which is in the adversarial region. Assumption B.1 means the feasible region of the optimization problem (3) is a nonempty set. By repeatedly reducing the radius R , the algorithm guarantees that the optimal tangent point is in the adversarial region, thereby making Assumption B.1 always hold. In addition, according to Assumption B.1, $\|\Pi_H(\mathbf{x})\| \geq R$ holds.

In Theorem 1, \mathbf{k} is an arbitrary point on the surface of the hemisphere $B \cap H_{\geq 0}$, so this proof mainly focuses on points in this region. In the following text, the hemisphere is denoted as $B' := B \cap H_{\geq 0}$, and its surface is denoted as $S' := S \cap H_{\geq 0}$ for brevity. Now, let us pick up any $\mathbf{k} \in S'^4$, and then the intersection point between the hyperplane H and the line passing through \mathbf{x} and \mathbf{k} is denoted as $\mathbf{y}_\mathbf{k}$. Then, $(\mathbf{y}_\mathbf{k}, \lambda)$ is the unique solution of the following equation system:

$$\begin{aligned} \mathbf{y}_\mathbf{k} &= \lambda \mathbf{k} + (1 - \lambda) \mathbf{x}, \\ \langle \mathbf{y}_\mathbf{k}, \mathbf{u} \rangle &= 0, \\ 0 &\leq \lambda \leq 1. \end{aligned} \quad (17)$$

Because the position of \mathbf{k} determines the distance between $\mathbf{y}_\mathbf{k}$ and \mathbf{x} , we can define the function $f(\mathbf{k}) := \|\mathbf{y}_\mathbf{k} - \mathbf{x}\|$ to represent the distance between \mathbf{x} and $\mathbf{y}_\mathbf{k}$.

B.2 Proof

To prove Theorem 1, we turn to prove the following lemma, which is equivalent to Theorem 1.

Lemma 1. *Let S' , f be defined as above, then minimizing f over the feasible region S' is equivalent to finding the point \mathbf{k} from the set $S' \cap C$ that is farthest away from H , *i.e.*,*

$$\arg \min_{\mathbf{k} \in S'} f(\mathbf{k}) = \arg \max_{\mathbf{k} \in (S' \cap C)} \langle \mathbf{k}, \mathbf{u} \rangle. \quad (18)$$

In addition, we can replace S' with B' in the above equation, and the optimal solution of $f(\mathbf{k})$ does not change. In other words, when the feasible region is B' , the optimal solution can be always obtained at the surface of B' . Thus, the following equation holds:

$$\arg \min_{\mathbf{k} \in S'} f(\mathbf{k}) = \arg \min_{\mathbf{k} \in B'} f(\mathbf{k}) = \arg \max_{\mathbf{k} \in (S' \cap C)} \langle \mathbf{k}, \mathbf{u} \rangle = \arg \max_{\mathbf{k} \in (B' \cap C)} \langle \mathbf{k}, \mathbf{u} \rangle. \quad (19)$$

Proof. By simplifying the original problem to a two-dimensional plane, the proof of Lemma 1 will be readily apparent. Let $V := \text{span}(\{\mathbf{x}, \mathbf{u}\})$ be the plane spanned by \mathbf{x} and \mathbf{u} . It is easy to observe B , S , C , B' , and S' are symmetrical about the plane V . Next, we will show that for any $\mathbf{k} \in B'$, there must exist a point $\mathbf{k}^* \in S' \cap V$ such that $f(\mathbf{k}^*) \leq f(\mathbf{k})$. To find the \mathbf{k}^* that satisfies the condition, we introduce the notation $\Pi_V : \mathbb{R}^n \mapsto V$ to denote the projection from \mathbb{R}^n to V .

Now, take any $\mathbf{k} \in B'$, and use \mathbf{k}'' to denote the mirror point of \mathbf{k} with respect to V , as shown in Fig. 8. The projection point $\Pi_V(\mathbf{k})$ is the midpoint of the line between \mathbf{k} and \mathbf{k}'' , *i.e.*, $\mathbf{k}'' = 2\Pi_V(\mathbf{k}) - \mathbf{k}$.

⁴Note that \mathbf{k} defined here may not be a tangent point on the ball.

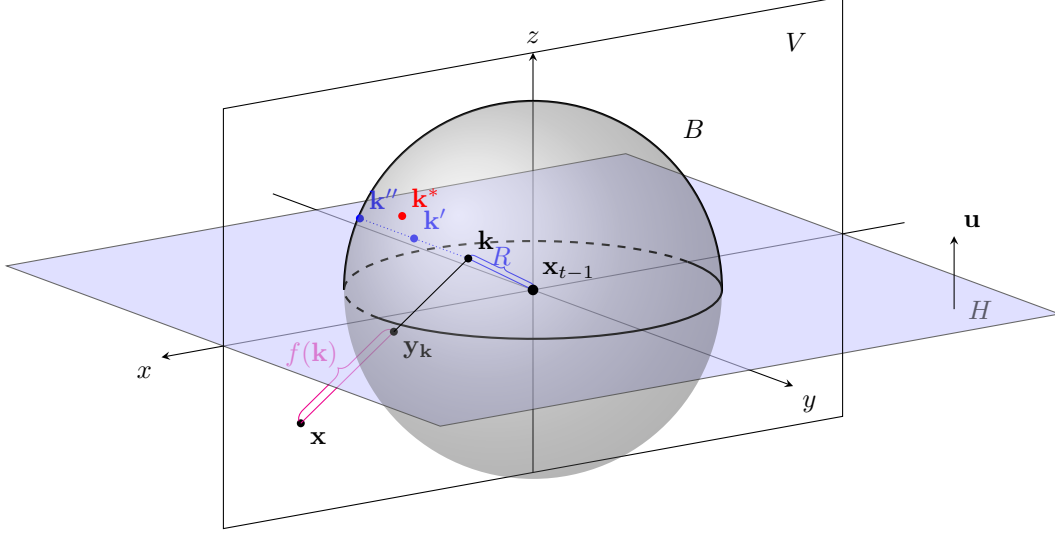


Figure 8: Illustration of the points used in proving Lemma 1, where \mathbf{k}'' is the mirror point of \mathbf{k} with respect to the plane V , and \mathbf{k}' is the projection of \mathbf{k} onto the plane V .

Note that if $\mathbf{k} \in V$, then \mathbf{k} , \mathbf{k}' and \mathbf{k}'' coincide. Since B' is symmetrical about the plane V , we have $\mathbf{k}'' \in B'$. Now since B' is the intersection of two convex sets B and $H_{\geq 0}$, we know that B' is also a convex set. Notice that $\Pi_V(\mathbf{k}) = \frac{1}{2} \cdot (\mathbf{k} + \mathbf{k}'')$ is a convex combination of \mathbf{k} and \mathbf{k}'' , and B' is a convex set, thus we conclude $\Pi_V(\mathbf{k}) \in B'$.

Now, we will show that we can ignore any point outside of V , thus restricting the problem to the two-dimensional plane V . Formally, the following inequality holds for any \mathbf{k} :

$$f(\Pi_V(\mathbf{k})) \leq f(\mathbf{k}). \quad (20)$$

The above inequality is easy to prove. Because $\mathbf{x} \in V$, we have $\|\Pi_V(\mathbf{y}_k - \mathbf{x})\| = \|\Pi_V(\mathbf{y}_k) - \mathbf{x}\|$. Therefore,

$$f(\Pi_V(\mathbf{k})) = \|\Pi_V(\mathbf{y}_k) - \mathbf{x}\| = \|\Pi_V(\mathbf{y}_k - \mathbf{x})\| \leq \|\mathbf{y}_k - \mathbf{x}\| = f(\mathbf{k}). \quad (21)$$

Now, we can focus on the plane V and find the optimal \mathbf{k}^* on it such that $f(\mathbf{k}^*) \leq f(\Pi_V(\mathbf{k}))$. Let us define C_0 to denote the convex cone with the point \mathbf{x} as the vertex, and its boundary is formed by all tangent lines from \mathbf{x} to B :

$$C_0 := \left\{ \mathbf{v} \in \mathbb{R}^n \mid \cos(\mathbf{v} - \mathbf{x}, -\mathbf{x}) \geq \sqrt{1 - \frac{R^2}{\|\mathbf{x}\|^2}} \right\}. \quad (22)$$

Let $\mathbf{k}' := \Pi_V(\mathbf{k})$ be the projection point of \mathbf{k} onto the plane V (see Fig. 9). Because $\mathbf{k}' \in B'$ and $\mathbf{k}' \in V$, we have $\mathbf{k}' \in \Pi_V(B')$. Now, we define $\mathbf{k}^* \in S' \cap C_0 \cap V$ to be the tangent point from \mathbf{x} to the semicircle $\Pi_V(B')$. We claim \mathbf{k}^* is the optimal one that attains the minimum $f(\mathbf{k}')$ among all \mathbf{k}' in $\Pi_V(B')$. We denote the angle between $-\mathbf{x}$ and \mathbf{u} as θ_1 , i.e., $\theta_1 := \arccos(\cos(-\mathbf{x}, \mathbf{u}))$. The angle between $-\mathbf{x}$ and $\mathbf{k}' - \mathbf{x}$ is denoted as θ_2 , i.e., $\theta_2 := \arccos(\cos(-\mathbf{x}, \mathbf{k}' - \mathbf{x}))$. Based on the position of \mathbf{k}' in $\Pi_V(B')$, there are two possible cases for the angle θ_2 , as shown in Fig. 9a and Fig. 9b, respectively. We discuss them separately below.

In the first case (Fig. 9a), $\mathbf{y}_{k'}$ and $\Pi_H(\mathbf{x})$ are on the same side of \mathbf{x}_{t-1} . By Assumption B.1, we know that $\|\Pi_H(\mathbf{x})\| \geq R$, so $\cos(-\mathbf{x}, \mathbf{u}) = \sqrt{1 - \|\Pi_H(\mathbf{x})\|^2 / \|\mathbf{x}\|^2} \leq \sqrt{1 - R^2 / \|\mathbf{x}\|^2}$. According to the definition of the convex cone C_0 , \mathbf{u} is outside C_0 . Notice that $\mathbf{x} \in C_0$ and $\mathbf{k}' \in \Pi_V(B')$, hence $\mathbf{k}' - \mathbf{x}$ is in the convex cone $\Pi_V(C_0)$. Therefore, based on the positions of the two vectors \mathbf{u} and $\mathbf{k}' - \mathbf{x}$ with respect to the cone $\Pi_V(C_0)$, we conclude that $\theta_1 \geq \theta_2$. In such case, the distance function is $f(\mathbf{k}') = \|\mathbf{y}_{k'} - \mathbf{x}\| = |\langle \mathbf{x}, \mathbf{u} \rangle| / \cos(\theta_1 - \theta_2)$, as shown in Fig. 9a. Because both \mathbf{x} and \mathbf{u} are fixed, the value of θ_1 is fixed. Therefore, the only way to minimize $f(\mathbf{k}')$ is to maximize θ_2 . Among all possible choices of \mathbf{k}' in $\Pi_V(B')$, the \mathbf{k}' that maximizes the angle θ_2 appears on

Table 4: The hyperparameters of HSJA.

Dataset	Hyperparameter	Value
CIFAR-10	γ , threshold of the binary search	1.0
	B_0 , the initial batch size for gradient estimation	100
	B_{\max} , the maximum batch size for gradient estimation	10,000
	the search method for step size	geometric progression
	number of iterations	64
ImageNet	γ , threshold of the binary search	1,000.0
	B_0 , the initial batch size for gradient estimation	100
	B_{\max} , the maximum batch size for gradient estimation	10,000
	the search method for step size	geometric progression
	number of iterations	64

Table 5: The hyperparameters of BA.

Hyperparameter	Value
maximum number of trials per iteration	25
number of iterations	1,200
spherical step size	0.01
source step size	0.01
step size adaptation multiplier	1.5
disable automatic batch size tuning	False
generate candidates and random numbers without using multithreading	False

Table 6: The hyperparameters of Sign-OPT.

Hyperparameter	Value
k , number of queries for estimating an approximate gradient	200
α , the update step size of the direction θ	0.2
β , used for the gradient estimation of θ and determining the stopping threshold of binary search	0.001
the number of iterations	1,000
the binary search’s stopping threshold of the CIFAR-10 dataset	$\frac{\beta}{500}$
the binary search’s stopping threshold of the ImageNet dataset	1×10^{-4}

Table 7: The hyperparameters of SVM-OPT.

Hyperparameter	Value
k , number of queries for estimating gradients	100
α , the step size of the gradient descent of θ	0.2
β , used for the gradient estimation of θ and determining the stopping threshold of binary search	0.001
the number of iterations	1,000
the binary search’s stopping threshold of the CIFAR-10 dataset	$\frac{\beta}{500}$
the binary search’s stopping threshold of the ImageNet dataset	1×10^{-4}

the hyperparameters of TA and G-TA to be the same with HSJA, *i.e.*, the same initial batch size B_0 and the same γ .

BA. Hyperparameters of BA [4] are listed in Table 5. In the experiments, we directly use the implementation of BA from Foolbox 2.0 [35, 36], and adopt a randomly selected image from the target class as the initialization in the targeted attack.

Sign-OPT and SVM-OPT. Hyperparameters of Sign-OPT [11] and SVM-OPT [11] are listed in Tables 6 and 7. We translate the implementation code into the PyTorch version for the experiments. In the experiments of targeted attacks, we set the initial direction θ_0 of Sign-OPT and SVM-OPT to the direction of a randomly selected image of the target class.

D Experimental Results

D.1 Limitation of Tangent Attack

The proposed approach supports all types of attacks, including both untargeted and targeted attacks under the both ℓ_2 and ℓ_∞ norm constraints. This is the strength of the proposed approach. However, in the ℓ_∞ norm attack, TA and G-TA obtain the similar performance to the baseline method HSJA. Because under the definition of the ℓ_∞ norm distance: $D_{\ell_\infty}(x, y) := \max_i(|x_i - y_i|)$, $i \in \{1, \dots, d\}$ (d is the image dimension), the intersection of the tangent line and the decision boundary may not be the one with the shortest ℓ_∞ norm distance to the original image. Therefore, searching the boundary sample along the tangent line cannot always outperform HSJA in the ℓ_∞ distortion.

Tables 8 and 9 demonstrate the experimental results of attacking against undefended models on the CIFAR-10 and ImageNet datasets.

Table 8: Mean ℓ_∞ distortions of different query budgets on the ImageNet dataset, where the radius ratio r is set to 1.1 in G-TA. BA is not applicable to the ℓ_∞ norm attack, hence it is not listed.

Target Model	Method	Targeted Attack						Untargeted Attack					
		@300	@1K	@2K	@5K	@8K	@10K	@300	@1K	@2K	@5K	@8K	@10K
Inception-v3	Sign-OPT [11]	0.550	0.509	0.474	0.422	0.395	0.384	1.077	0.726	0.513	0.335	0.280	0.260
	SVM-OPT [11]	0.558	0.512	0.476	0.423	0.397	0.385	1.079	0.763	0.526	0.336	0.280	0.260
	HSJA [7]	0.370	0.330	0.289	0.211	0.169	0.147	0.305	0.236	0.174	0.093	0.069	0.059
	TA	0.370	0.330	0.291	0.216	0.172	0.149	0.304	0.234	0.173	0.093	0.068	0.059
	G-TA	0.365	0.325	0.289	0.211	0.170	0.147	0.307	0.237	0.174	0.093	0.069	0.061
Inception-v4	Sign-OPT [11]	0.540	0.495	0.458	0.404	0.377	0.365	1.183	0.803	0.570	0.375	0.313	0.291
	SVM-OPT [11]	0.547	0.498	0.460	0.406	0.379	0.367	1.181	0.842	0.588	0.381	0.319	0.296
	HSJA [7]	0.357	0.324	0.287	0.215	0.175	0.152	0.336	0.257	0.185	0.091	0.060	0.048
	TA	0.354	0.328	0.294	0.221	0.182	0.161	0.337	0.264	0.196	0.103	0.073	0.062
	G-TA	0.362	0.326	0.292	0.220	0.178	0.156	0.338	0.263	0.194	0.102	0.073	0.062
SENet-154	Sign-OPT [11]	0.530	0.476	0.426	0.356	0.322	0.306	0.807	0.585	0.439	0.305	0.263	0.247
	SVM-OPT [11]	0.538	0.480	0.429	0.357	0.322	0.307	0.807	0.608	0.444	0.306	0.262	0.246
	HSJA [7]	0.347	0.288	0.249	0.176	0.139	0.119	0.253	0.195	0.141	0.071	0.048	0.039
	TA	0.346	0.289	0.251	0.181	0.142	0.123	0.253	0.196	0.141	0.071	0.047	0.038
	G-TA	0.339	0.283	0.246	0.174	0.137	0.119	0.255	0.194	0.140	0.071	0.048	0.039
ResNet-101	Sign-OPT [11]	0.542	0.490	0.442	0.370	0.334	0.317	0.643	0.479	0.367	0.260	0.223	0.210
	SVM-OPT [11]	0.550	0.492	0.444	0.371	0.335	0.319	0.642	0.494	0.370	0.258	0.220	0.206
	HSJA [7]	0.340	0.283	0.247	0.179	0.143	0.125	0.197	0.140	0.098	0.049	0.034	0.028
	TA	0.340	0.282	0.246	0.180	0.143	0.125	0.196	0.145	0.109	0.064	0.050	0.044
	G-TA	0.342	0.282	0.246	0.180	0.145	0.127	0.197	0.147	0.110	0.065	0.052	0.046

Table 9: Mean ℓ_∞ distortions of different query budgets on the CIFAR-10 dataset, where the radius ratio r is set to 1.5 in G-TA. BA is not applicable to the ℓ_∞ norm attack, and thus it is not listed.

Target Model	Method	Targeted Attack						Untargeted Attack					
		@300	@1K	@2K	@5K	@8K	@10K	@300	@1K	@2K	@5K	@8K	@10K
PyramidNet-272	Sign-OPT [11]	0.388	0.299	0.226	0.135	0.100	0.087	0.287	0.172	0.103	0.059	0.049	0.046
	SVM-OPT [11]	0.390	0.299	0.226	0.134	0.099	0.087	0.286	0.173	0.104	0.059	0.049	0.046
	HSJA [7]	0.218	0.155	0.112	0.057	0.039	0.032	0.133	0.056	0.034	0.016	0.012	0.011
	TA	0.219	0.154	0.112	0.057	0.039	0.032	0.134	0.057	0.035	0.017	0.013	0.011
	G-TA	0.218	0.153	0.115	0.061	0.044	0.037	0.168	0.129	0.117	0.100	0.092	0.088
GDAS	Sign-OPT [11]	0.386	0.322	0.265	0.164	0.119	0.100	0.304	0.258	0.222	0.184	0.170	0.165
	SVM-OPT [11]	0.389	0.325	0.267	0.164	0.118	0.100	0.304	0.257	0.219	0.181	0.168	0.163
	HSJA [7]	0.210	0.147	0.112	0.060	0.040	0.031	0.049	0.029	0.020	0.011	0.009	0.008
	TA	0.214	0.151	0.115	0.062	0.041	0.032	0.049	0.029	0.020	0.011	0.009	0.008
	G-TA	0.209	0.150	0.116	0.063	0.043	0.035	0.089	0.072	0.067	0.058	0.054	0.052
WRN-28	Sign-OPT [11]	0.380	0.295	0.224	0.128	0.092	0.080	0.196	0.119	0.080	0.052	0.046	0.043
	SVM-OPT [11]	0.382	0.296	0.223	0.128	0.093	0.080	0.201	0.121	0.079	0.052	0.045	0.043
	HSJA [7]	0.185	0.106	0.070	0.032	0.021	0.018	0.090	0.031	0.020	0.012	0.010	0.009
	TA	0.186	0.107	0.070	0.031	0.021	0.018	0.090	0.030	0.020	0.012	0.010	0.009
	G-TA	0.183	0.106	0.071	0.032	0.024	0.022	0.143	0.103	0.092	0.078	0.072	0.069
WRN-40	Sign-OPT [11]	0.379	0.292	0.218	0.126	0.091	0.079	0.284	0.195	0.125	0.052	0.043	0.041
	SVM-OPT [11]	0.381	0.293	0.220	0.126	0.092	0.079	0.273	0.190	0.120	0.057	0.045	0.041
	HSJA [7]	0.194	0.111	0.072	0.032	0.022	0.019	0.084	0.030	0.020	0.012	0.010	0.009
	TA	0.195	0.112	0.073	0.032	0.022	0.019	0.082	0.029	0.020	0.012	0.010	0.009
	G-TA	0.191	0.109	0.072	0.033	0.025	0.022	0.139	0.101	0.091	0.077	0.071	0.068

The results of Tables 8 and 9 show that HSJA, TA and G-TA obtain the similar average ℓ_∞ distortions. Therefore, although the proposed approach is applicable to ℓ_∞ norm attack, the performance is similar to that of the baseline method HSJA.

D.2 Experimental Results of Attacks against Defense Models

We also conduct experiments by using ℓ_∞ norm attacks to break five defense models, and the experimental results are shown in Table 10. The conclusion drawn from this table is the same as that in Tables 8 and 9: TA and G-TA obtain the similar performance with HSJA in ℓ_∞ norm attacks.

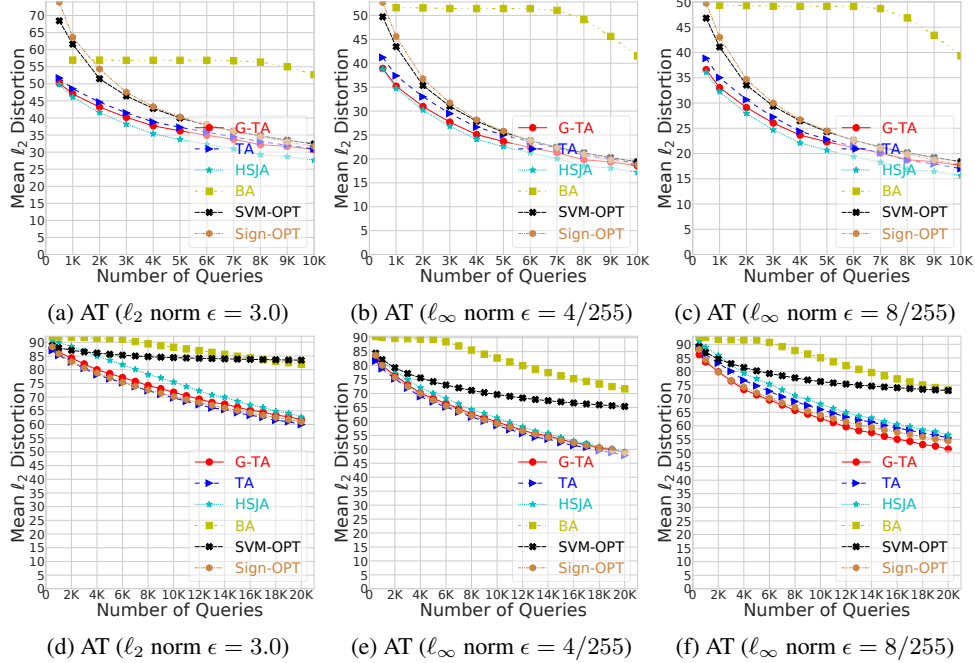
Table 10: The experimental results of performing ℓ_∞ norm attacks against the defense models on the CIFAR-10 dataset, where the radius ratio r is set to 1.5 in G-TA.

Target Model	Method	Untargeted Attack					
		@300	@1K	@2K	@5K	@8K	@10K
AT [30]	Sign-OPT [11]	0.717	0.499	0.383	0.288	0.262	0.252
	SVM-OPT [11]	0.719	0.498	0.382	0.287	0.261	0.251
	HSJA [7]	0.181	0.145	0.121	0.090	0.080	0.075
	TA	0.184	0.147	0.121	0.090	0.079	0.075
	G-TA	0.186	0.149	0.123	0.091	0.080	0.076
TRADES [46]	Sign-OPT [11]	0.747	0.528	0.406	0.309	0.282	0.273
	SVM-OPT [11]	0.743	0.534	0.409	0.308	0.281	0.271
	HSJA [7]	0.194	0.162	0.137	0.106	0.095	0.090
	TA	0.195	0.163	0.138	0.107	0.095	0.090
	G-TA	0.193	0.160	0.137	0.107	0.096	0.091
JPEG [18]	Sign-OPT [11]	0.307	0.293	0.281	0.263	0.255	0.252
	SVM-OPT [11]	0.301	0.288	0.275	0.256	0.249	0.246
	HSJA [7]	0.094	0.086	0.078	0.066	0.061	0.058
	TA	0.093	0.087	0.080	0.067	0.061	0.058
	G-TA	0.092	0.085	0.079	0.068	0.066	0.065
Feature Distillation [28]	Sign-OPT [11]	0.346	0.330	0.314	0.289	0.277	0.272
	SVM-OPT [11]	0.354	0.338	0.323	0.297	0.284	0.279
	HSJA [7]	0.090	0.087	0.080	0.069	0.064	0.061
	TA	0.089	0.086	0.079	0.070	0.063	0.060
	G-TA	0.089	0.085	0.079	0.071	0.068	0.067
Feature Scatter [45]	Sign-OPT [11]	0.545	0.344	0.223	0.138	0.118	0.111
	SVM-OPT [11]	0.550	0.344	0.222	0.137	0.116	0.110
	HSJA [7]	0.202	0.137	0.104	0.062	0.048	0.042
	TA	0.202	0.137	0.104	0.062	0.048	0.042
	G-TA	0.212	0.138	0.104	0.062	0.049	0.043

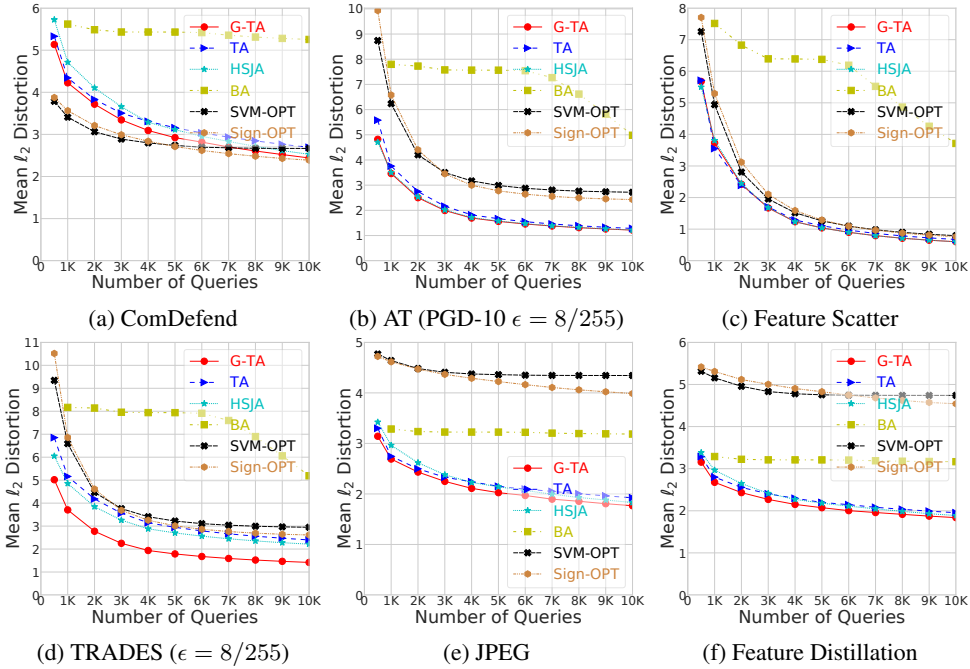
Next, we conduct experiments by using ℓ_2 norm attack to break different defense models on the CIFAR-10 and ImageNet datasets. In the CIFAR-10 dataset, we select six types of defense models:

- Adversarial Training (AT) [30]: the most effective defense method, which uses adversarial examples as the training data to obtain the robust classifier.
- TRADES [46]: an improved AT that optimizes a regularized surrogate loss.
- JPEG [18]: a standard image compression algorithm based on the discrete cosine transform, which can remove the adversarial perturbations, thereby providing some degree of defense.
- Feature Distillation [28]: a defense method based on the improved JPEG image compression. Its defense mechanism is divided into two steps. Firstly, it filters out adversarial perturbations by using a semi-analytical method. Secondly, it restores the classification accuracy of benign images by using a DNN-oriented quantization process.
- Feature Scatter [45]: a feature scattering-based AT method, which is an unsupervised approach for generating adversarial examples during the training.
- ComDefend [23]: a defense model that consists of a compression CNN and a reconstruction CNN to transform the adversarial image into its clean version to defend against attacks.

In the ImageNet dataset, we directly use the publicly available AT models for experiments, all of which use the ResNet-50 networks as their backbones. The pre-trained weights can be downloaded from <https://github.com/MadryLab/robustness>. In the experiments, we set the radius ratio r of G-TA to 1.5. Fig. 10 demonstrates the results. The results show that G-TA (the semi-ellipsoid version) almost outperforms the TA (the hemisphere version) in all cases, which demonstrates its superiority in the attacks of defense models. However, In untargeted attacks, the baseline method HSJA outperforms TA and G-TA. We conjecture that it is because the classification decision boundaries of the AT models on the ImageNet dataset are extremely curved in untargeted attacks, resulting in the better performance of HSJA. In targeted attacks, both TA and G-TA outperform HSJA in the attacks of different AT models. These results indicate that our approach is more suitable for the targeted attack. Another



(a) AT (ℓ_2 norm $\epsilon = 3.0$) (b) AT (ℓ_∞ norm $\epsilon = 4/255$) (c) AT (ℓ_∞ norm $\epsilon = 8/255$)
 (d) AT (ℓ_2 norm $\epsilon = 3.0$) (e) AT (ℓ_∞ norm $\epsilon = 4/255$) (f) AT (ℓ_∞ norm $\epsilon = 8/255$)
 Figure 10: Experimental results of ℓ_2 norm attacks against adversarial trained ResNet-50 networks on the ImageNet dataset, where the first row (Figs. 10a, 10b, 10c) shows the results of untargeted attacks, and the second row (Figs. 10d, 10e, 10f) shows the results of targeted attacks.



(a) ComDefend (b) AT (PGD-10 $\epsilon = 8/255$) (c) Feature Scatter
 (d) TRADES ($\epsilon = 8/255$) (e) JPEG (f) Feature Distillation
 Figure 11: Experimental results of the ℓ_2 norm untargeted attacks against defense models on the CIFAR-10 dataset, where all defense models adopt the backbone of ResNet-50 network.

interesting finding is that SVM-OPT performs better in untargeted attacks while Sign-OPT performs better in targeted attacks. We will explore the reasons for these results in the future work.

Figs. 11 and 12 show the experimental results of untargeted and targeted attacks on the CIFAR-10 dataset, respectively. In the results of untargeted attacks (Fig. 11), G-TA performs best in the attacks of TRADES, JPEG and Feature Distillation. When the target models are AT and Feature Scatter, the

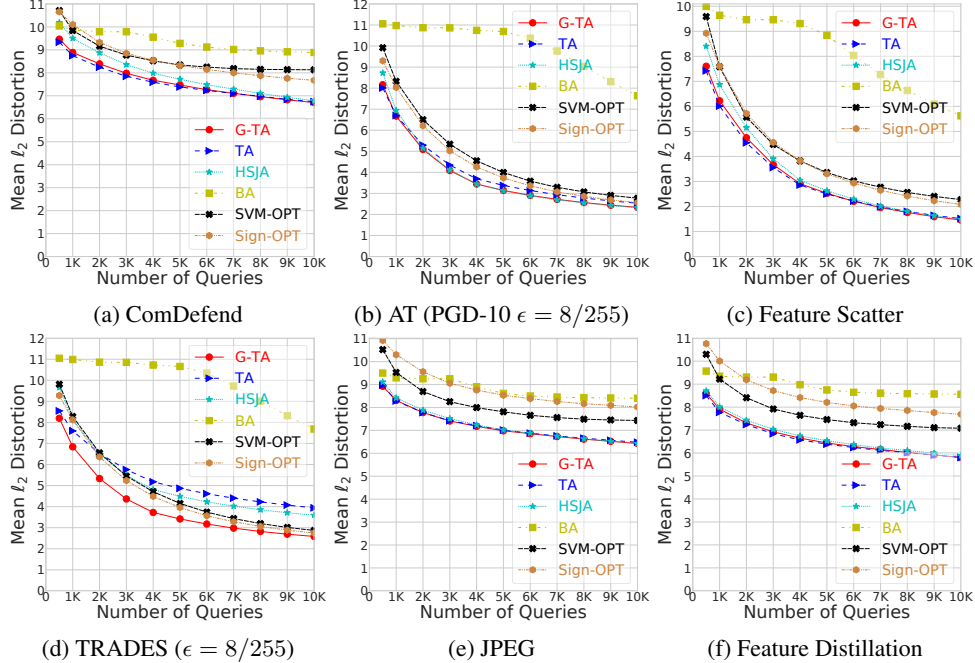


Figure 12: Experimental results of the l_2 norm targeted attacks against defense models on the CIFAR-10 dataset, where all defense models adopt the backbone of ResNet-50 network.

performance of G-TA is similar to that of the baseline attack method HSJA. These results demonstrate the advantage of G-TA, which can surpass HSJA when attacking different defense models.

In addition, in the results of targeted attacks (Fig. 12), G-TA performs best in the attack of TRADES, and its performance is similar to TA when attacking other defense models.

D.3 Distributions of Distortions across Different Adversarial Examples

So far, all the experimental results only show the average l_2 distortion of 1,000 adversarial examples. To check the distortion of each adversarial example in more detail, we extract the l_2 distortions of 20 samples from HSJA, TA and G-TA. These samples are selected from 1,000 images in the following way: from the 1st image to the 1,000th image, we select one image for every 50 images. Fig. 13 shows the distributions of l_2 distortions across 20 adversarial examples on the ImageNet dataset, where the 1st image’s “image number index” is 0. The results indicate that the l_2 distortions obtained by TA and G-TA are uniformly better than that of the baseline method HSJA. Thus, our approach can obtain better l_2 distortions on different adversarial examples, not just on specific samples.

D.4 Experimental Results of Median Distortions

In this section, we report the median l_2 distortions of different query budgets on the CIFAR-10 and ImageNet datasets. Tables 11 and 12 show the experimental results. We can draw the following conclusions based on the results.

(1) TA and G-TA perform better in attacking high-resolution images, *i.e.*, the images of the ImageNet dataset. The median l_2 distortions of Table 11 are larger than that of Table 12, because the high-resolution images of the ImageNet dataset lead to larger l_2 distortions.

(2) TA is more effective in the targeted attacks while G-TA performs better in untargeted ones. We speculate that it is because the adversarial region of the target class is narrower and more scattered, resulting in a smoother decision boundary. Thus, TA is more suitable for targeted attacks.

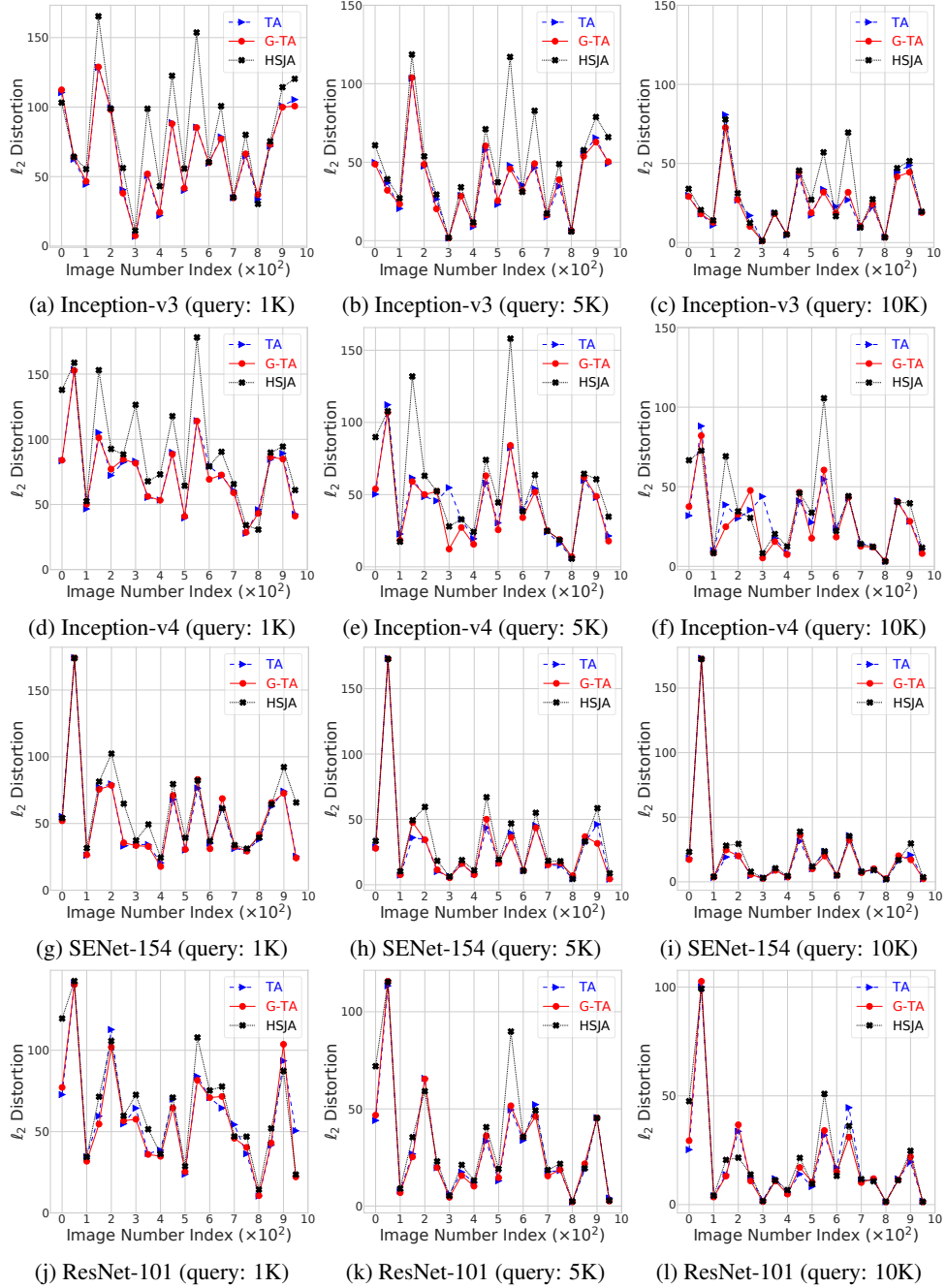


Figure 13: Comparisons of ℓ_2 distortions across 20 adversarial examples in targeted attacks of the ImageNet dataset.

Table 11: Median ℓ_2 distortions of different query budgets on the ImageNet dataset. “-” denotes no adversarial example is found in this query budget.

Target Model	Method	Targeted Attack						Untargeted Attack					
		@300	@1K	@2K	@5K	@8K	@10K	@300	@1K	@2K	@5K	@8K	@10K
Inception-v3	BA [4]	105.513	101.877	101.056	97.481	81.269	73.524	-	109.507	103.637	96.340	79.027	58.924
	Sign-OPT [11]	96.905	83.215	66.601	43.350	31.036	25.380	115.140	73.319	38.327	12.761	8.277	6.808
	SVM-OPT [11]	93.649	77.838	63.631	42.897	31.838	26.322	114.879	59.343	30.627	12.085	8.352	7.025
	HSJA [7]	106.341	92.114	79.225	47.469	30.624	23.838	105.702	53.880	32.684	12.360	7.829	6.227
	TA	96.612	75.610	62.573	38.226	25.892	19.993	95.302	50.878	31.833	11.921	7.464	6.030
	G-TA	97.449	75.499	62.484	38.886	26.004	20.091	96.006	50.283	30.819	11.759	7.524	5.957
Inception-v4	BA [4]	104.275	101.115	99.872	96.700	79.412	71.387	-	116.855	112.335	104.557	85.044	64.123
	Sign-OPT [11]	95.388	81.865	66.159	42.871	31.241	25.798	121.725	77.838	40.465	14.268	8.924	7.153
	SVM-OPT [11]	92.640	77.616	62.949	42.552	31.142	26.238	120.407	64.600	33.960	13.586	9.035	7.535
	HSJA [7]	104.969	90.371	78.103	47.340	31.404	24.270	109.422	60.356	37.302	14.191	8.790	6.934
	TA	96.808	74.829	61.974	37.155	26.128	21.184	101.170	55.876	36.403	14.176	8.592	6.814
	G-TA	95.563	75.889	62.404	38.457	26.495	21.069	101.254	56.682	35.801	13.769	8.612	6.765
SENet-154	BA [4]	75.653	72.327	71.420	68.293	52.332	44.391	-	75.355	70.498	65.186	51.950	38.164
	Sign-OPT [11]	70.500	59.556	45.566	27.062	18.218	14.400	65.524	42.690	23.688	9.054	5.331	4.194
	SVM-OPT [11]	72.029	55.637	44.009	27.378	19.014	15.526	65.957	35.596	20.549	8.760	5.368	4.332
	HSJA [7]	72.589	60.361	49.487	25.718	14.929	12.197	70.043	34.697	21.811	8.098	4.482	3.707
	TA	66.285	51.012	40.475	21.590	13.293	10.782	64.784	34.034	22.269	7.636	4.273	3.555
	G-TA	66.077	51.852	41.065	21.946	13.461	10.899	65.460	33.740	21.849	7.739	4.333	3.572
ResNet-101	BA [4]	76.772	72.674	71.761	68.231	54.847	47.785	-	63.568	59.384	55.402	42.777	29.097
	Sign-OPT [11]	72.361	62.383	48.664	30.089	20.752	16.478	53.757	35.070	19.035	8.442	5.929	4.999
	SVM-OPT [11]	73.758	58.716	47.496	30.443	21.502	17.535	52.471	29.225	16.469	8.245	6.043	5.259
	HSJA [7]	73.422	60.175	49.443	26.504	16.035	12.661	54.869	24.971	15.161	6.084	3.787	3.237
	TA	69.511	55.389	44.343	24.500	14.778	11.802	51.829	24.748	15.162	5.941	3.698	3.203
	G-TA	69.117	56.275	44.315	24.316	15.133	11.946	51.871	24.928	14.866	5.864	3.658	3.164

Table 12: Median ℓ_2 distortions of different query budgets on the CIFAR-10 dataset.

Target Model	Method	Targeted Attack						Untargeted Attack					
		300	@1K	@2K	@5K	@8K	@10K	300	@1K	@2K	@5K	@8K	@10K
PyramidNet-272	BA [4]	8.240	7.711	7.697	6.013	3.938	3.068	-	5.133	4.268	4.060	2.471	1.460
	Sign-OPT [11]	7.900	6.050	3.796	1.441	0.762	0.549	3.821	1.952	0.980	0.345	0.232	0.196
	SVM-OPT [11]	8.870	6.432	4.199	1.651	0.894	0.655	3.777	1.956	0.877	0.363	0.235	0.202
	HSJA [7]	7.616	4.013	2.109	0.589	0.384	0.325	3.935	1.022	0.587	0.294	0.224	0.201
	TA	7.650	3.874	2.071	0.599	0.380	0.318	3.758	1.028	0.589	0.289	0.223	0.197
	G-TA	7.452	3.980	2.110	0.602	0.387	0.324	3.938	1.033	0.590	0.288	0.224	0.198
GDAS	BA [4]	8.098	7.568	7.554	5.774	3.301	2.396	-	2.626	2.409	2.286	1.541	1.015
	Sign-OPT [11]	7.947	6.418	4.166	1.514	0.669	0.457	2.067	1.331	0.766	0.298	0.209	0.176
	SVM-OPT [11]	9.138	7.242	5.090	2.103	1.043	0.673	2.043	1.230	0.674	0.302	0.211	0.183
	HSJA [7]	7.687	3.061	1.383	0.435	0.298	0.254	1.905	0.674	0.429	0.232	0.185	0.168
	TA	7.667	3.024	1.380	0.435	0.296	0.253	1.932	0.690	0.425	0.228	0.185	0.169
	G-TA	7.728	3.104	1.385	0.430	0.298	0.253	1.883	0.665	0.428	0.226	0.182	0.167
WRN-28	BA [4]	8.317	7.789	7.764	5.493	2.199	1.293	-	3.900	3.332	3.167	1.361	0.732
	Sign-OPT [11]	7.737	5.188	2.816	0.797	0.439	0.354	2.679	1.298	0.723	0.281	0.214	0.191
	SVM-OPT [11]	9.054	5.697	3.317	0.981	0.511	0.398	2.627	1.279	0.627	0.288	0.218	0.198
	HSJA [7]	6.446	2.064	1.005	0.443	0.339	0.306	2.497	0.697	0.442	0.264	0.224	0.208
	TA	6.518	2.018	0.988	0.428	0.337	0.306	2.606	0.682	0.431	0.262	0.225	0.210
	G-TA	6.444	2.060	1.000	0.439	0.341	0.306	2.538	0.682	0.444	0.261	0.223	0.209
WRN-40	BA [4]	8.181	7.760	7.722	5.482	2.193	1.363	-	3.773	3.187	3.045	1.321	0.726
	Sign-OPT [11]	7.782	5.285	2.895	0.845	0.455	0.369	2.510	1.213	0.679	0.265	0.194	0.173
	SVM-OPT [11]	9.042	5.835	3.400	1.030	0.549	0.420	2.500	1.251	0.611	0.272	0.198	0.179
	HSJA [7]	6.578	2.183	1.040	0.439	0.338	0.305	2.470	0.702	0.453	0.256	0.214	0.198
	TA	6.747	2.100	0.983	0.435	0.337	0.305	2.584	0.680	0.434	0.254	0.215	0.201
	G-TA	6.514	2.069	1.014	0.438	0.339	0.306	2.453	0.695	0.441	0.255	0.213	0.199